Gonzalez, ED.; Gil, LV.; Kugelmeyer, CL.; Amigó, V.; Mastelaro, VR.; Rovere, CA.; Nascente, PA. (2022). Effect of Zr content on the physicochemical, electrochemical, and biological properties of Ti80Nb20-based alloys. Materials Today Communications. 32:1-10. https://doi.org/10.1016/j.mtcomm.2022.104069

Highlights

- The effect of the addition of Zr to the Ti-Nb_{20} system was evaluated.
- The addition of Zr favored the stabilization of the β phase, and a reduction in both the elastic modulus and the hardness.
- Electrochemical tests in the Ringer's and NaCl solutions indicated an enrichment of both Nb_2O_5 and ZrO_2 surface oxides, and a depletion of TiO_2.
- The best set of properties was presented by the $Ti_{60}Nb_{20}Zr_{20}$ alloy.

Graphical Abstract

Alloys of Ti_{80-x}-Nb_{20}-Zr_x (x = 5, 10, 20, 30, and 40 at.%) were produced by electric arc casting. The results show that the addition of Zr causes a decrease in both the elastic modulus and the hardness of the molten alloys The increase in the Zr content caused a microstructural difference between the phases All alloys with different Zr amounts showed wide passivation regions and no sign of pitting in the potential range that is characteristic of the human body. The Ti-Nb-Zr alloys showed good compatibility in cell growth tests, with the best results for the 20 at.% Zr alloy.

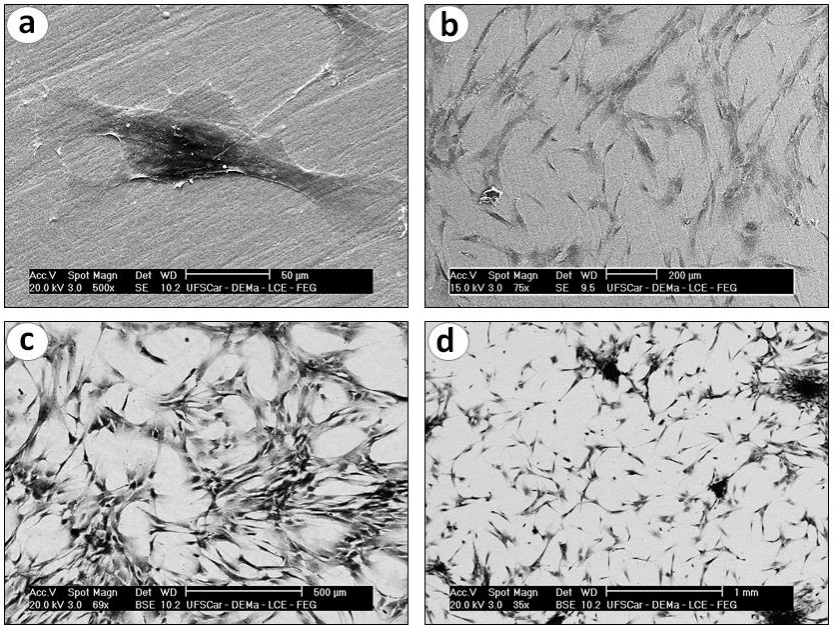

BSE/SEM micrographs showing the cell adhesion on the Ti-Nb-Zr alloys after 72 h of incubation: a) $Ti_{75}Nb_{20}Zr_5$, b) $Ti_{60}Nb_{20}Zr_{20}$, c) $Ti_{50}Nb_{20}Zr_{30}$, and d) $Ti_{40}Nb_{20}Zr_{40}$.

Figure 2

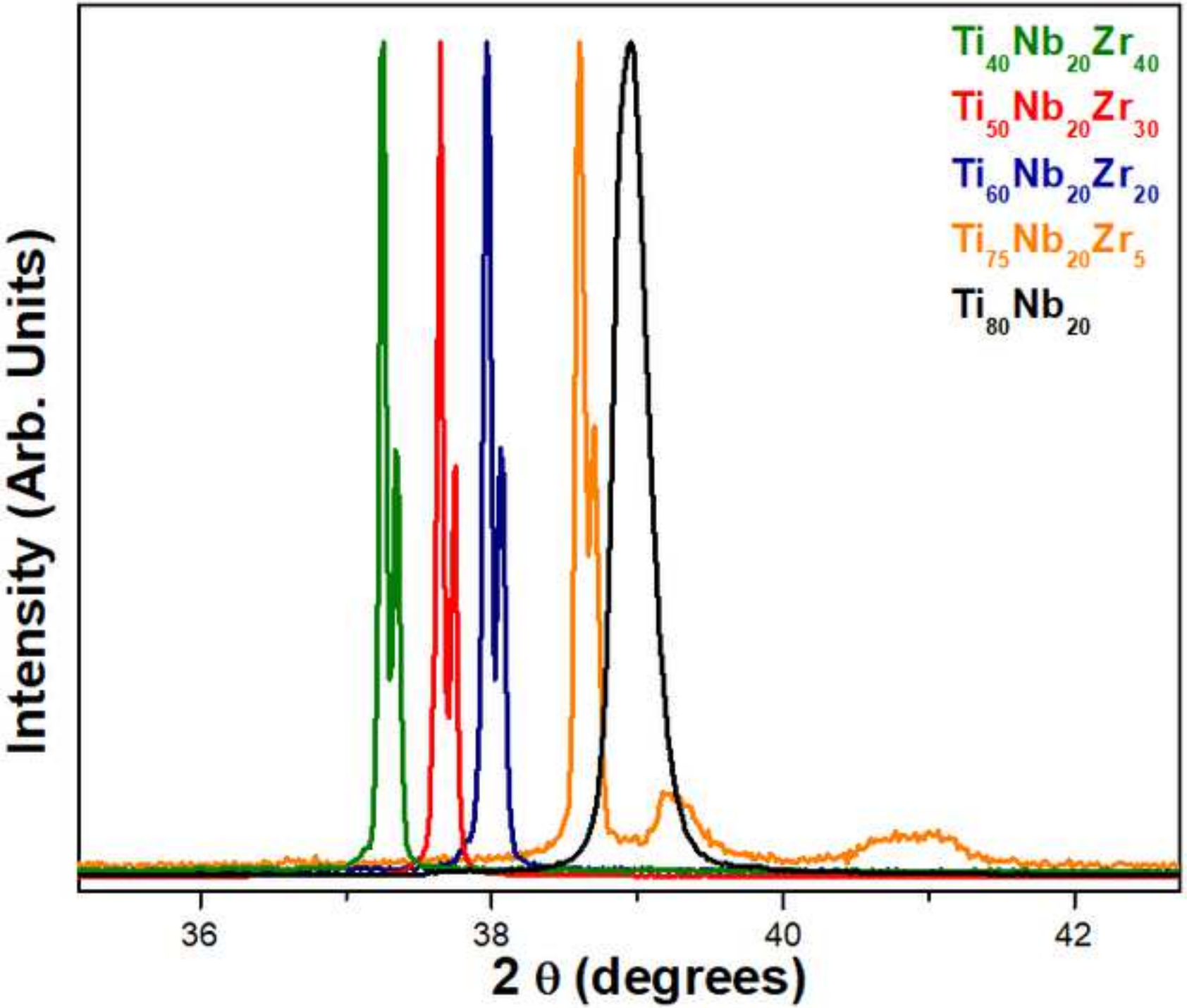

Figure 3

Click here to access/download;Figure;Figure 3.tif

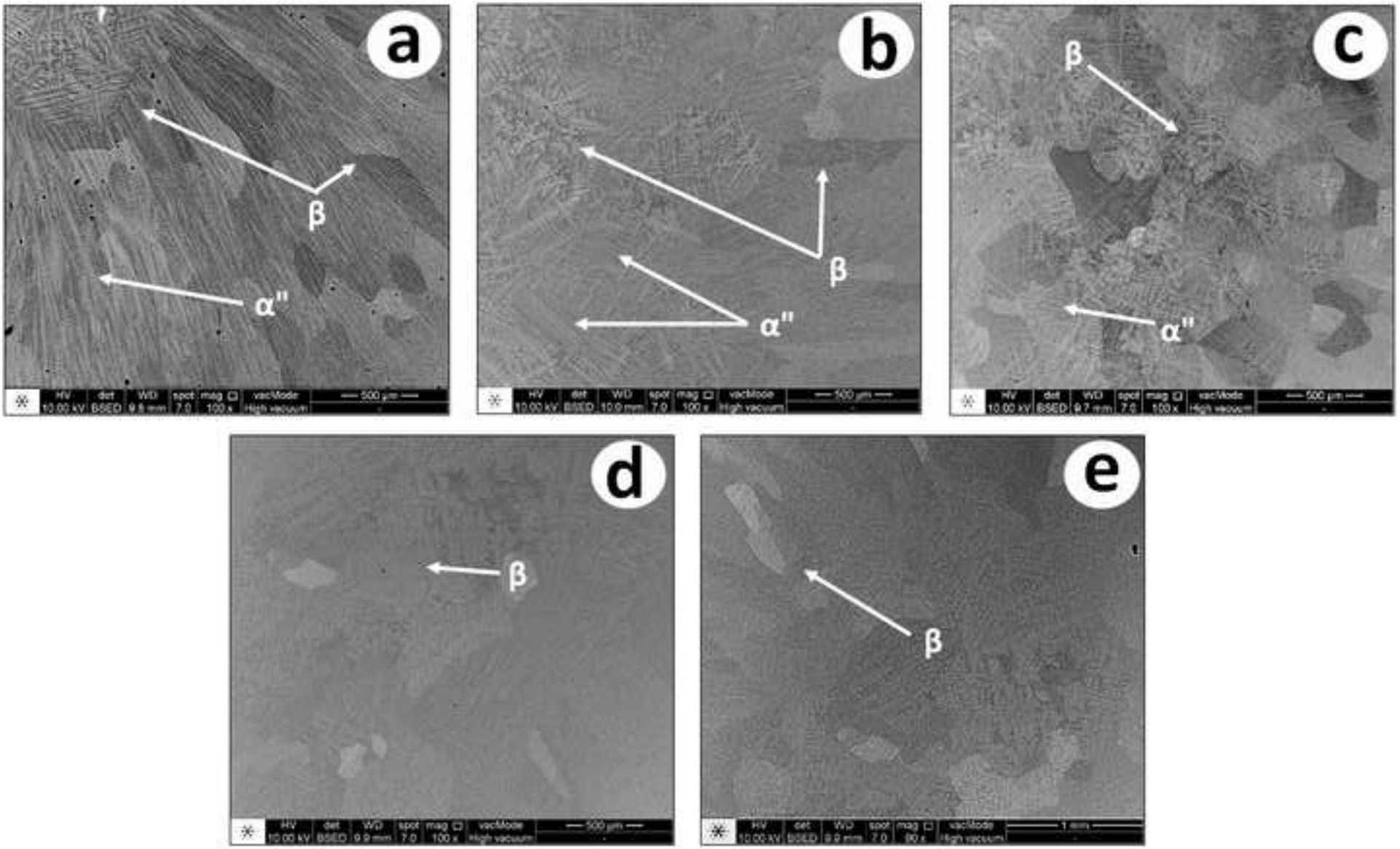

Figure 4

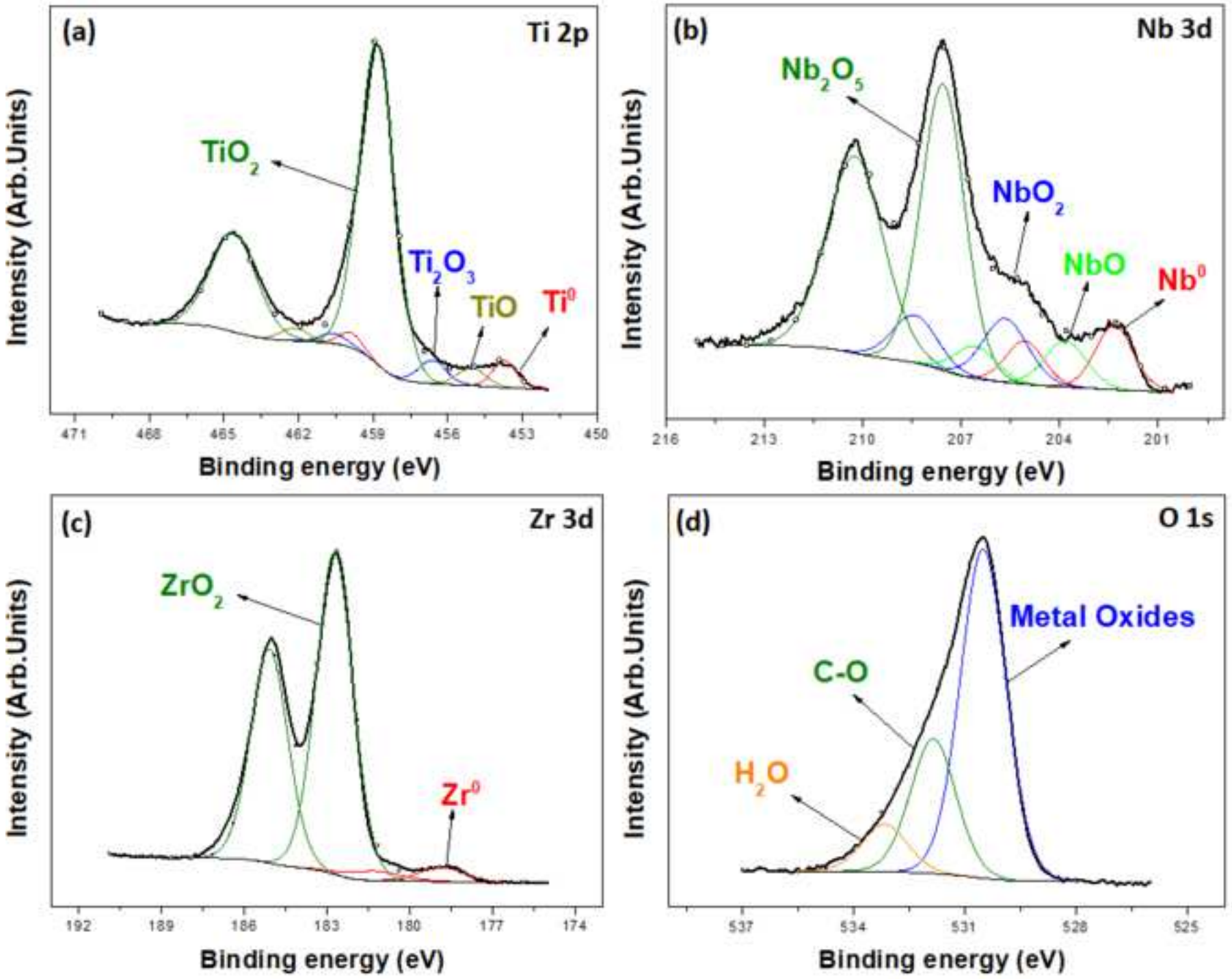

Figure 5

Click here to access/download;Figure;Figure 5 - corrected.tif

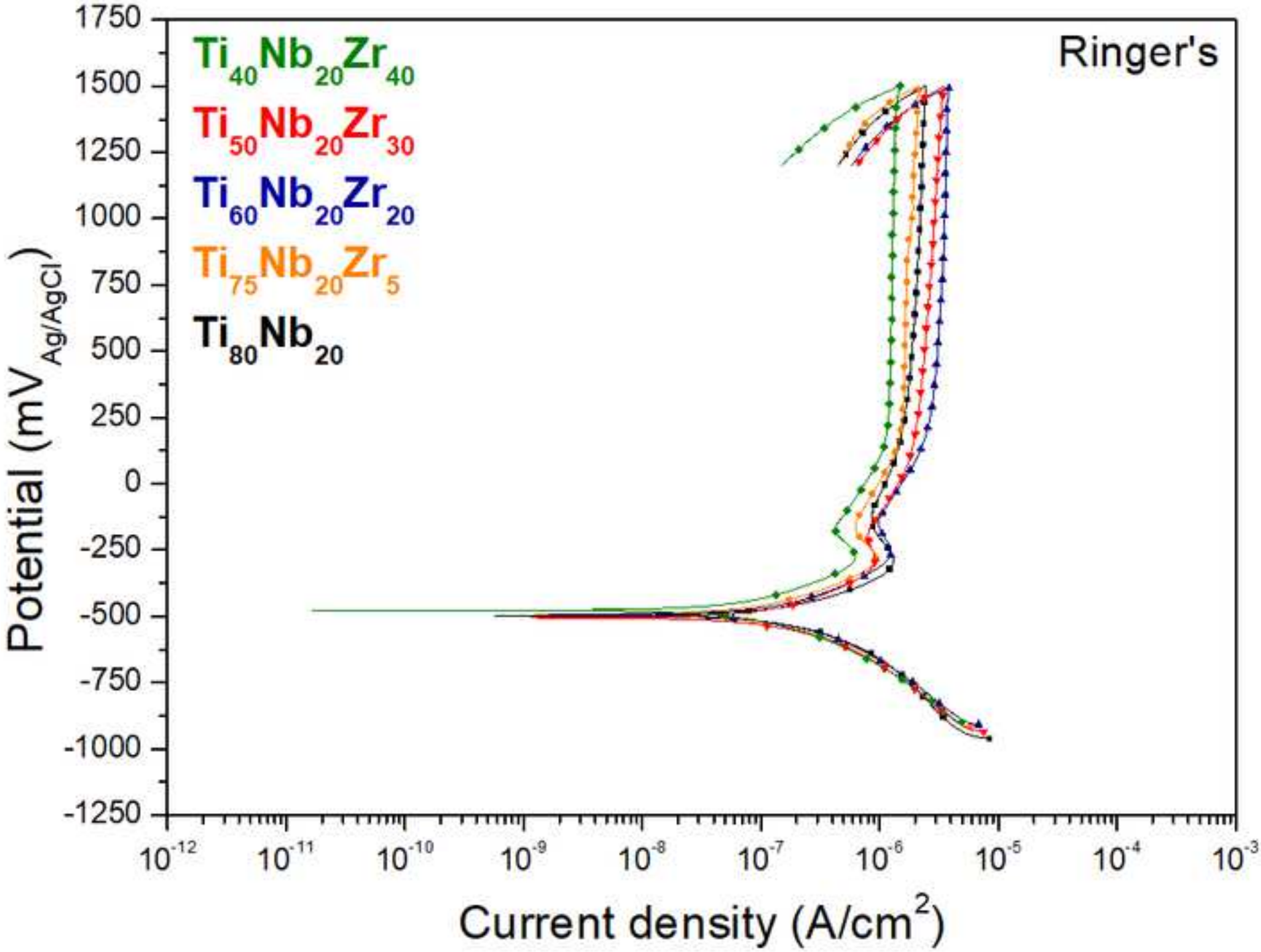

Figure 6

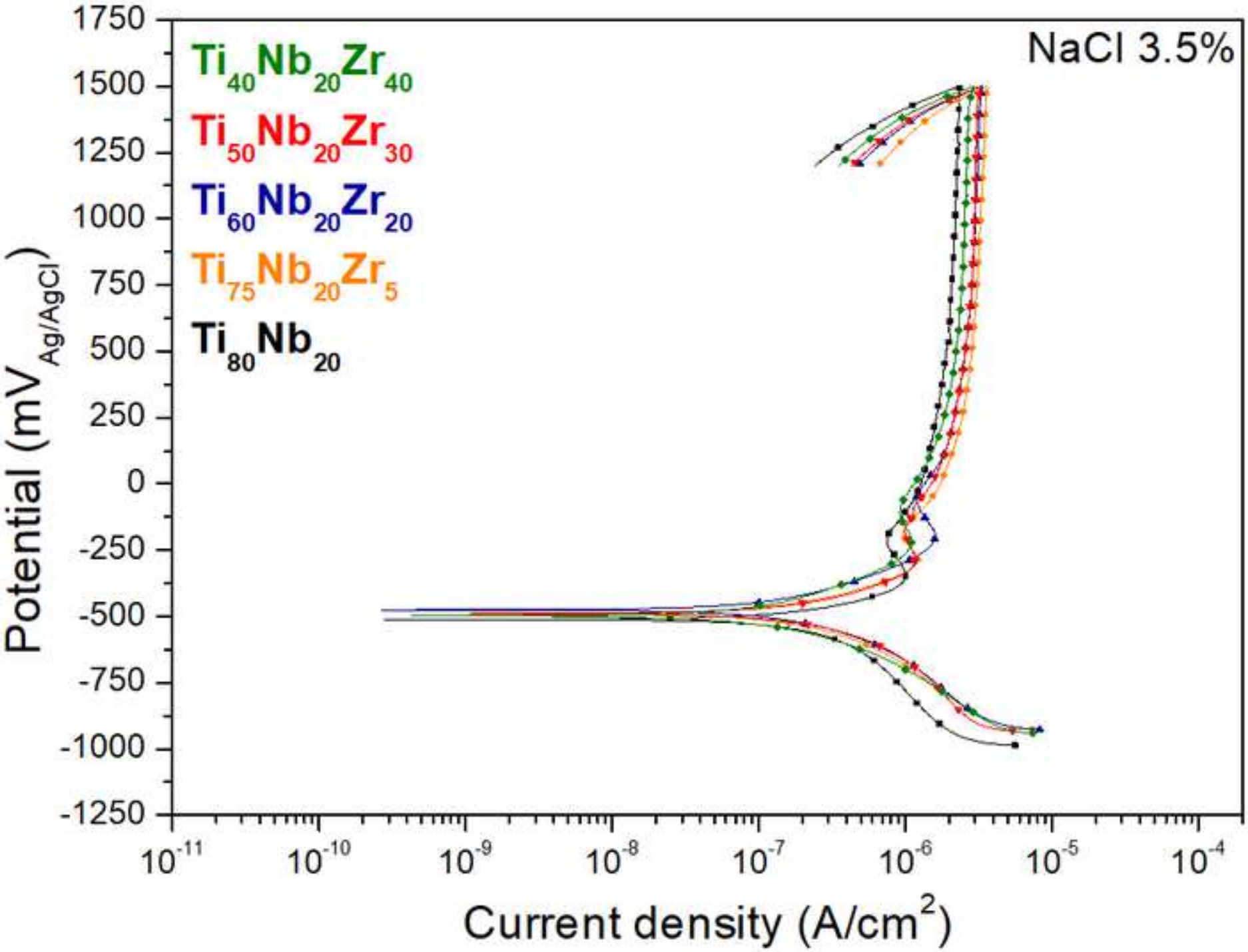

Figure 7

Click here to access/download;Figure;Figure 7.tif

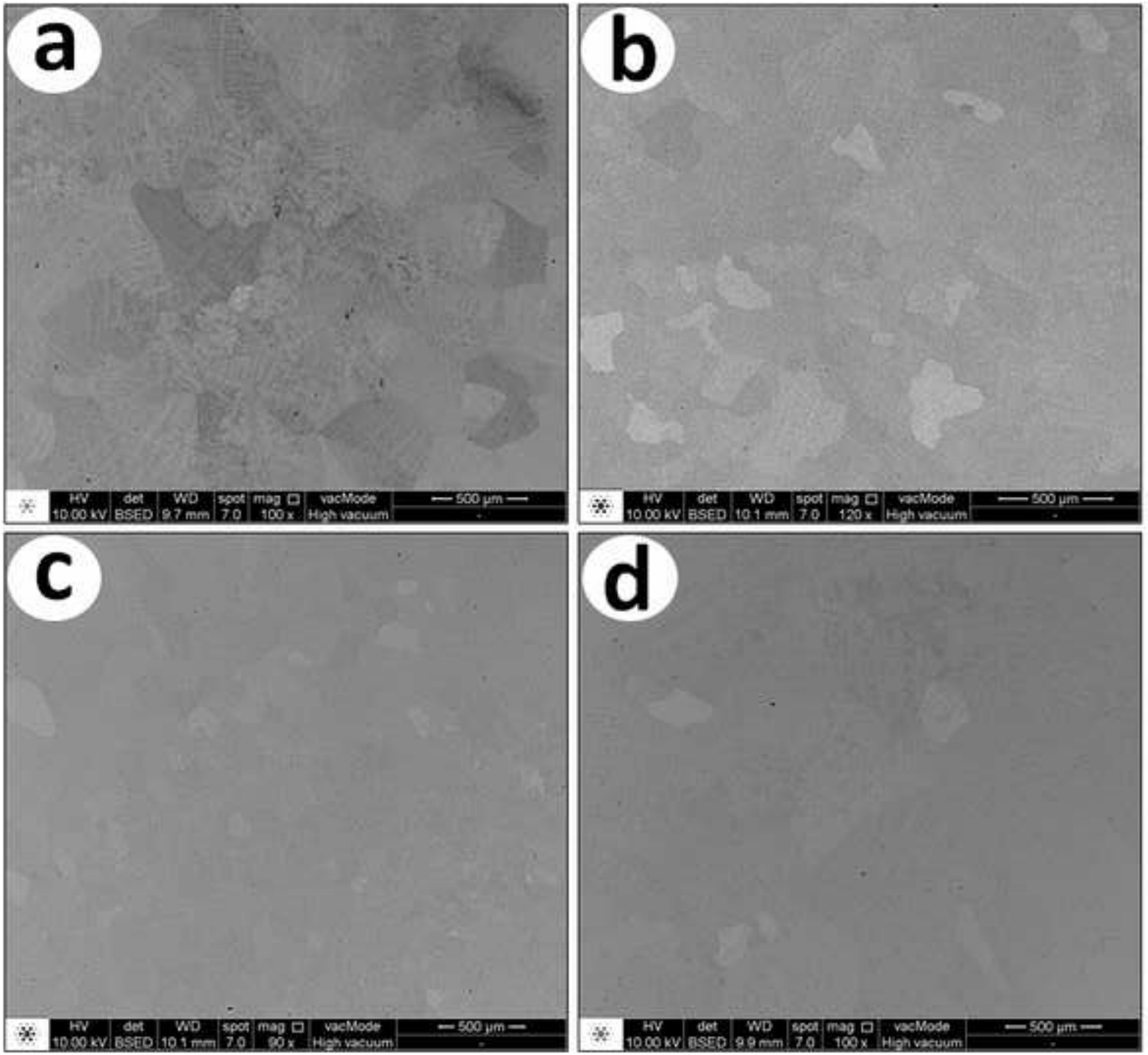

Figure 8

Click here to access/download;Figure;Figure 8.tif

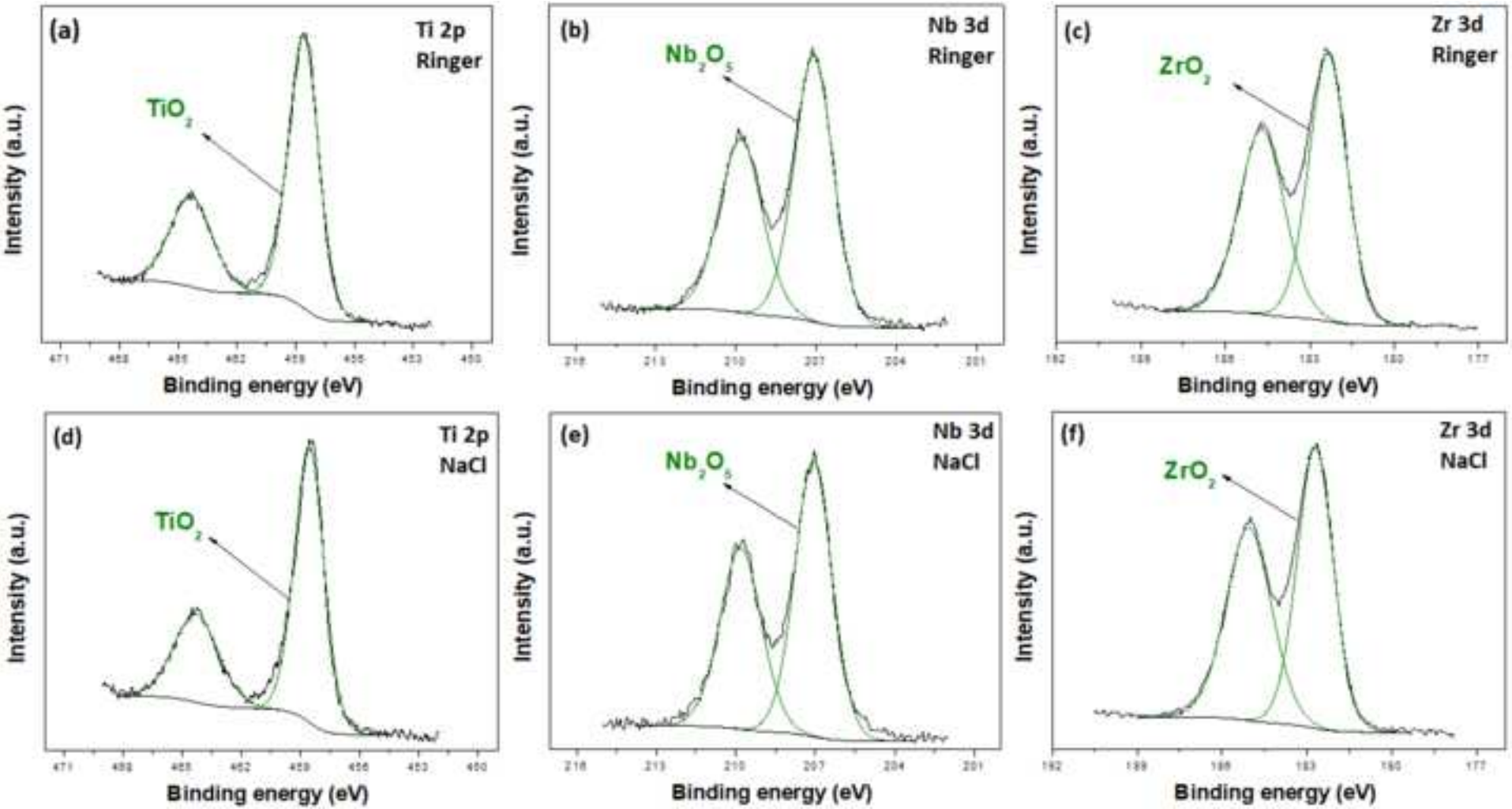

Figure 9

Click here to access/download;Figure;Figure 9.tif

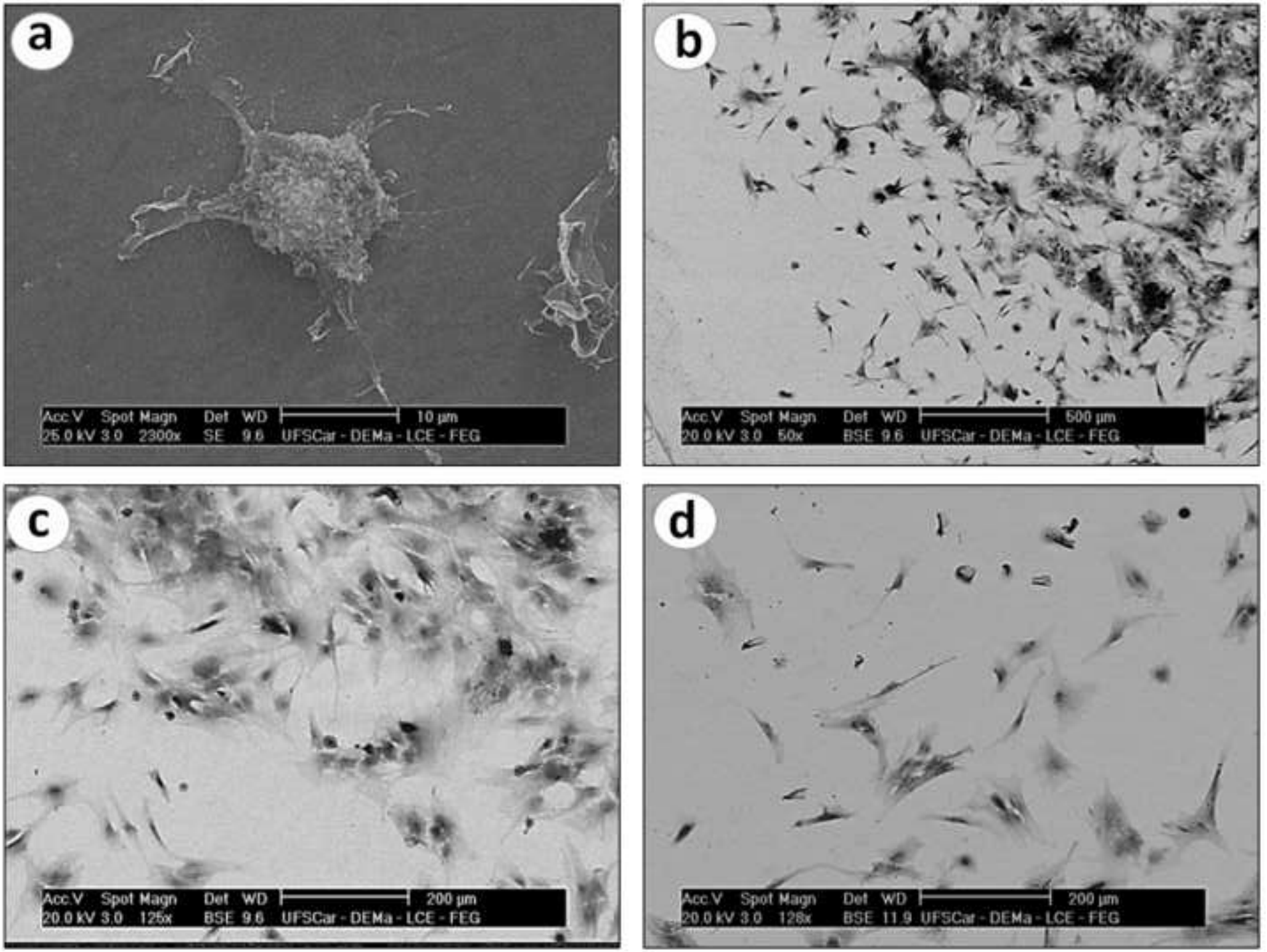

Figure 10

Click here to access/download;Figure;Figure 10.tif

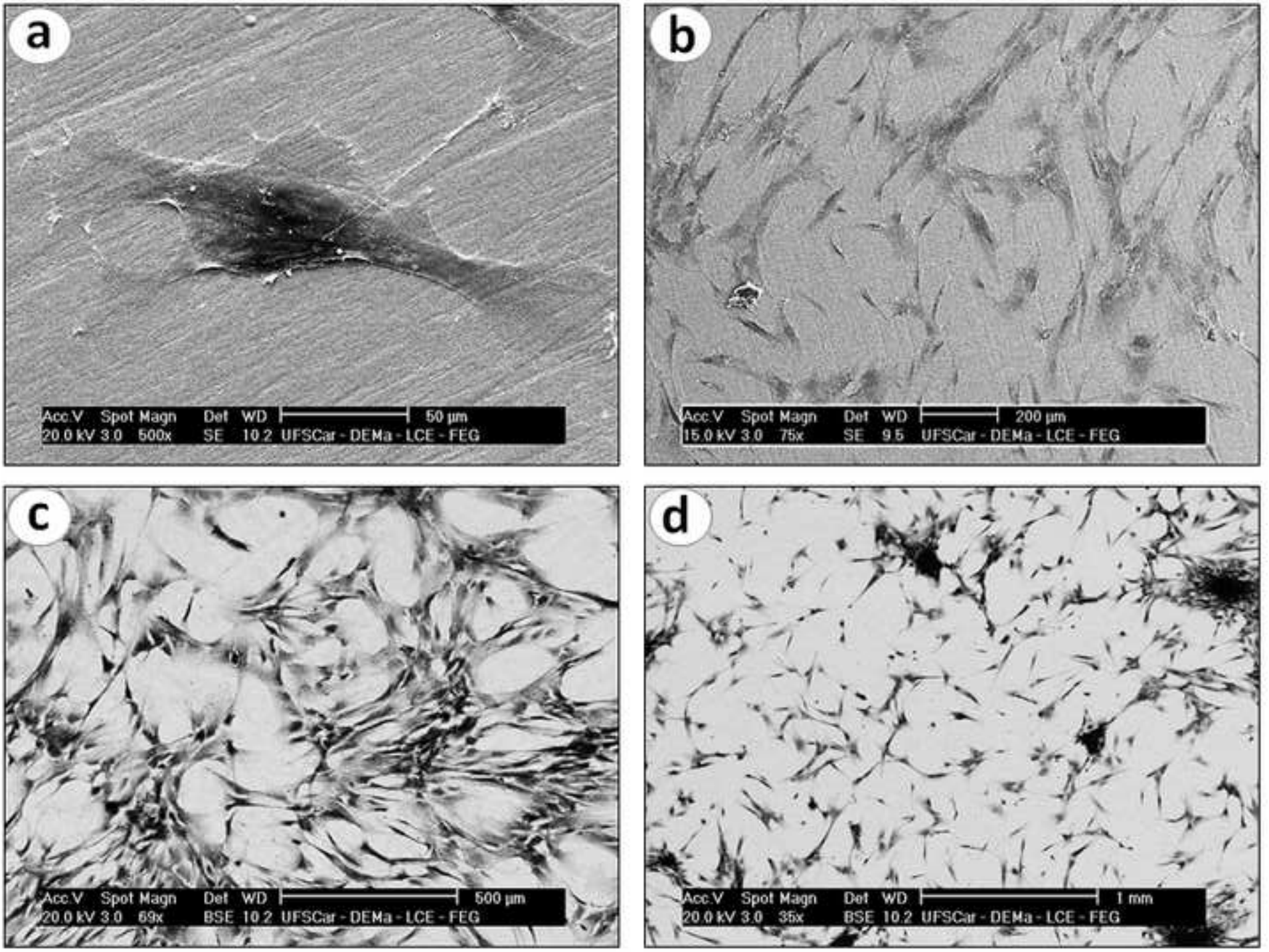

Figure 11

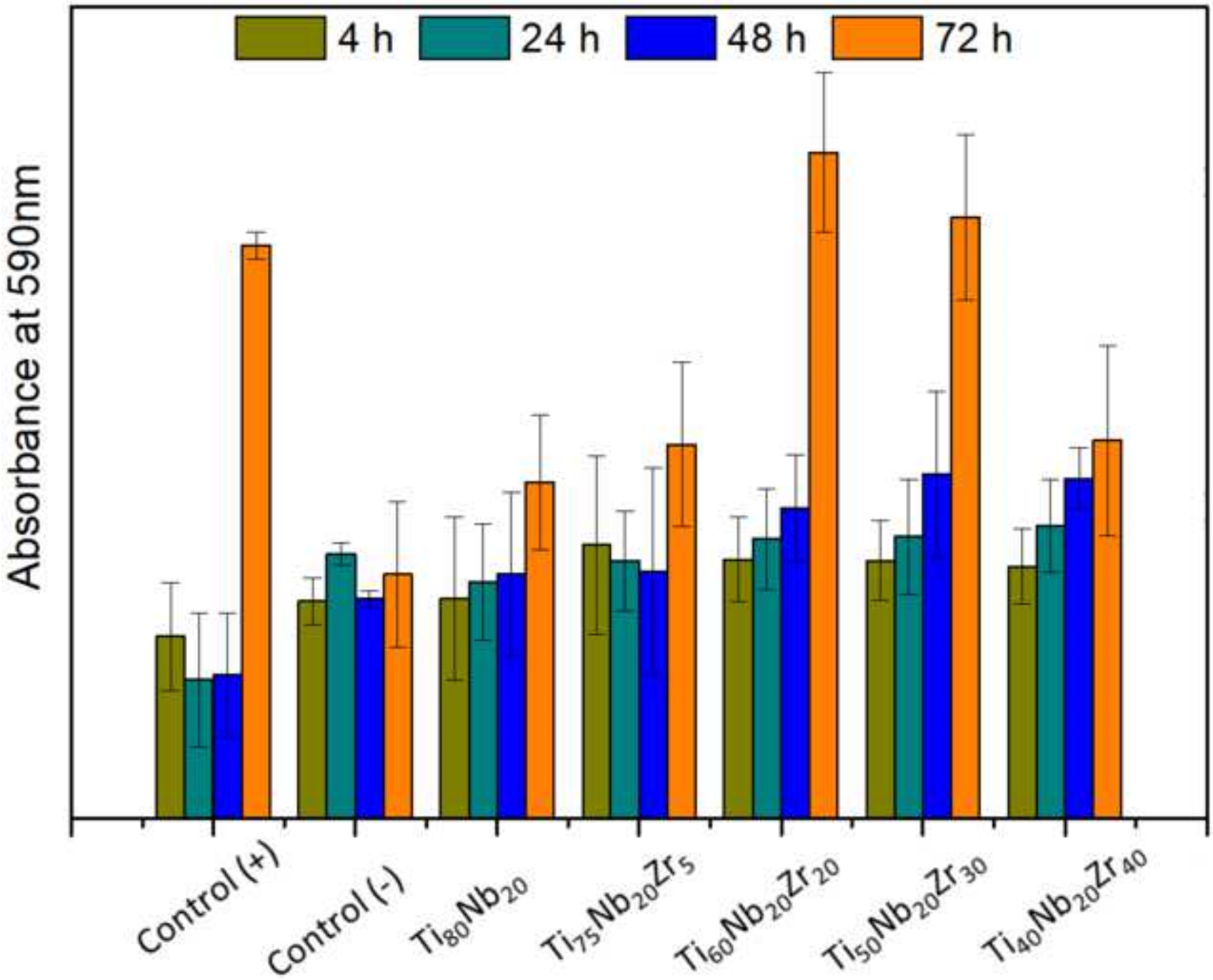

Figure 1

Click here to access/download;Figure;Figure 1 - D.tif

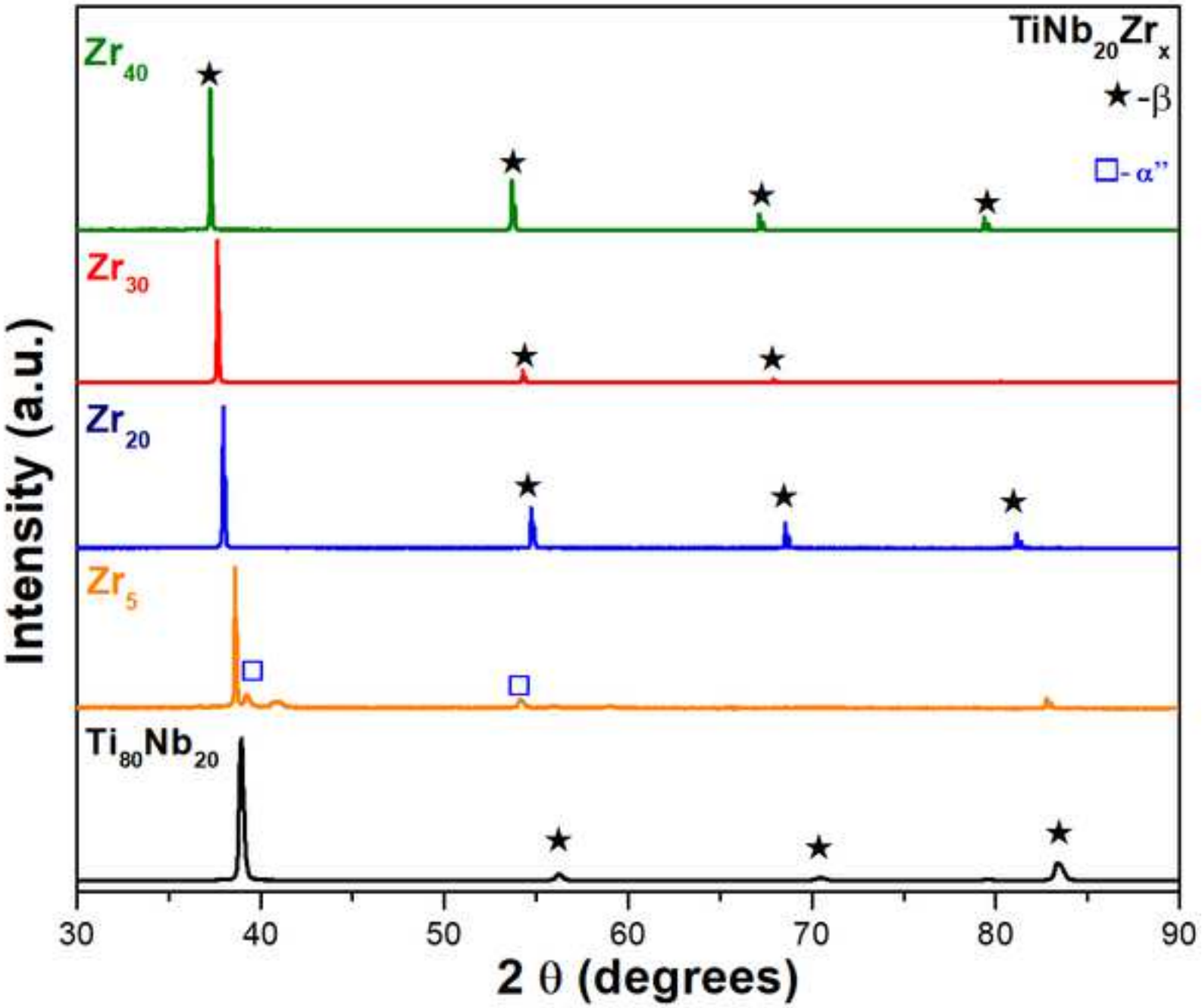

Effect of Zr content on the physicochemical, electrochemical, and biological properties of $Ti_{80}Nb_{20}$-based alloys

E. David Gonzalez [a], Liseth V. G. Gil [b], Cristie. L. Kugelmeier [a], Vicente Amigó-Borras [c], Valmor. R. Mastelaro [d], Carlos A. D. Rovere [a, e], Pedro A. P. Nascente [a, e, *]

[a] Universidade Federal de São Carlos, Programa de Pós-Graduação em Ciência e Engenharia de Materiais, CEP 13565-905, São Carlos, SP, Brazil;

[b] Universidade Federal de São Carlos, Programa de Pós-Graduação em Engenharia Química, CEP 13565-905, São Carlos, SP, Brazil

[c] Universitat Polytècnica de València (UPV), Instituto de Tecnología de Materiales, Camino de Vera, 46022 Valencia, Spain.

[d] Universiade de São Paulo, Instituto de Física de São Carlos, CEP 13560-590, São Carlos, SP, Brazil

[e] Universidade Federal de São Carlos, Departamento de Engenharia de Materiais, CEP 13565-905, São Carlos, SP, Brazil.

(*) Corresponding author, e-mail: nascente@ ufscar.br

ABSTRACT

The β-Ti alloys have become very attractive in the area of biomedical materials due to their corrosion resistance, biocompatibility, and low elastic modulus as compared with other materials. In this context, the Ti-Nb-Zr ternary system has gained more interest because Zr acts as secondary β-Ti stabilizing element when it is added together with β-stabilizing element such as Nb or Mo. According to the d-electron theory, the higher the Zr content, the lower elastic modulus values are obtained, which would allow to produce alloys with low elastic modulus, corrosion resistance, and shape memory. However, determining the ideal amount of Zr in a Ti-Nb-Zr alloy is still a matter of investigation. In this work, alloys with a nominal chemical composition of Ti_{80-x}-Nb_{20}-Zr_x (x = 5, 10, 20, 30, and 40 at.%) were produced by electric arc casting. The results show that the addition of Zr causes a decrease in both the elastic modulus and the hardness of the molten alloys, reaching values of 50.5 GPa for a sample with 40 at.% Zr. The increase in the Zr content caused a microstructural difference between the phases, and the α" phase was detected for the $Ti_{80}Nb_{20}$, $Ti_{75}Nb_{20}Zr_5$, and $Ti_{60}Nb_{20}Zr_{20}$ alloys. The X-ray photoelectron spectroscopy (XPS) analysis revealed that the environment influences the Ti-Nb-Zr surfaces, showing the growth of oxide layers, mainly Ti, Zr and, to a lesser extent, Nb oxides. All alloys with different Zr amounts showed wide passivation regions and no sign of pitting in the potential range that is characteristic of the human body. The Ti-Nb-Zr alloys showed good compatibility in cell growth tests, with the best results for the 20 at.% Zr alloy, and a decrease in biocompatibility for higher Zr amounts due to reactions of Zr^{4+} with body fluids.

Keywords: Ti-Nb-Zr alloys, biomaterials, biocompatibility, β-Ti.

1. Introduction

Titanium and its alloys have been one of the most studied metallic materials for biomedical applications due to their good mechanical properties, corrosion resistance, and biocompatibility, as compared to stainless steels and cobalt based alloys, which are traditionally used in orthopedic implants [1–3]. β-phase Ti alloys stand out due to their low elastic modulus, which is an intrinsic property of the material that is associated with the charge transfer between the implant and the tissue around it, both in volume and on the surface [4–8]. For comparison, the elastic modulus values for AISI 316L stainless steel and Co-Cr alloys, which are the most used metallic biomaterials in implants, are 210 and 210-240 GPa, respectively, while for the Ti-based alloys are in the range of 40 to 110 GPa, much closer to cortical bones (15-30 GPa) [8, 9]. Among the β-Ti alloys, the Ti-Nb system is attractive due to the beneficial influence of Nb on the Ti properties. Nb is a non-toxic and non-allergenic element, and its addition to Ti causes a decrease in the elastic modulus [3]. The Ti-Nb system also presents superelasticity (shape memory), for 22-25 at% Nb, and superplasticity, for 25.5-27 at% Nb, [5, 10, 11]. Different authors have reported that the composition range between 16 and 26 at.% shows the best balance of mechanical properties, biocompatibility, and corrosion resistance, in addition to large stress-induced deformations [12–15]. However, for Nb amount in the range of 13 to 23 at.%, the metastable ω-Ti phase can be formed, and it exhibits the highest elastic modulus among all phases formed in titanium alloys [13-16]. Therefore, the precipitation of this ω phase leads to an increase in both the elastic modulus and the hardness [13, 15, 17]. In order to control the mechanical properties, the microstructure, and the obtained phases, ternary elements are added to the Ti-Nb system, with zirconium being the most attractive one due mainly to the suppression of the ω and the martensitic phases, reducing the transformation temperature Ms [18, 19]. Moreover, the addition of Zr decreases the critical stress for sliding deformation, which increases the deformation induced by the phase transformation, improving the superelastic behavior and the shape memory effect [20-23]. Although Zr is considered a neutral element for the stabilization of the β phase, when added together with a β stabilizing element, such as Nb, Ta, and Mo, it increases the β stabilizing effect [20, 24-28]. The addition of Zr in alloys with a Nb content greater than 20 at. % also produces a refinement of the interdendritic spacing, generating a more homogeneous structure that improves the corrosion resistance [29] and facilitates the recrystallization processes [30].

All these advantages have converted the Ti-Nb-Zr alloys into one of the most studied systems regarding biomedical applications, with the aim of establishing the optimal composition and processing type. The methods of calculating the molecular orbital (d-electron theory) [18, 21, 31, 32] and the molybdenum equivalent [7, 33, 34] have allowed for the development of many combinations of concentrations and processes, most of which are focused on the effect of thermomechanical processes [18, 26, 30, 35-43] and the impact of replacing Nb with Zr on superelastic properties [20, 22, 44-48]. However, the study of the metallurgical aspects for high Zr concentrations (upper right region of the Bo, Md diagram) as well as the effect of replacing Ti by Zr on mechanical, electrochemical, and biological properties have been little explored. Thus, the purpose of the present work was to evaluate the effect of the addition of Zr on the physicochemical, electrochemical, and biological properties of the Ti-Nb_{20} system.

2. Experimental Setup and Methodology

$Ti_{80}Nb_{20}$, $Ti_{75}Nb_{20}Zr_5$, $Ti_{60}Nb_{20}Zr_{20}$, $Ti_{50}Nb_{20}Zr_{30}$, and $Ti_{40}Nb_{20}Zr_{40}$ alloy ingots were produced from pure metals using arc melting with a suction casting system, model Edmund Bulher D-72411. Bars having 12 mm in diameter and 110 mm in length were obtained, and these bars were subsequently cut to form discs with a thickness of 2 mm for the different analyzes. This casting process has high cooling rates (water quenching), being similar to the solubilization process that facilitates obtaining the single β phase in these alloys [46].

The structural characterization was carried out using a Bruker diffractometer, model D8 Advance ECO, in Bragg-Brentano mode (θ / 2θ), using Cu Kα radiation (λ = 1.5405 Å), an acceleration voltage of 40 kV, and a current of 20 mA. Peak indexing was done with the help of the Inorganic Crystal Structure Database (ICSD).

The hardness measurements were performed according to the ASTM E384 standard, using a Shimadzu microdurometer, model HMV-G 20ST, the load applied load was 500 gram-force (gf) with a standardized load time of 15 s. The elastic modules were evaluated using the impulse excitation technique according to the ASTM E1876 standard. The equipment used was an ATCP Sonelastic with a sample holder suitable for small samples connected to a computer, with dedicated software for signal processing developed by the manufacturer. Two types of cylindrical specimens were used:

the first one having 12 mm in diameter and 110 mm in length and the second one having 5 mm in diameter and 32 mm in length.

The scanning electron microscopy (SEM) morphological characterization was used to observe the microstructures of the alloys, as well as the sample surfaces after the cell growth tests. The SEM analyzes were performed using a FEI Inspect S50 microscope, to which was attached an energy dispersive spectroscopy (EDS) system having an Oxford Link Tentafet X-ray detector.

The compositions of the passive layers before and after the electrochemical polarization tests were assessed by X-ray photoelectron spectroscopy (XPS) analyzes using a Scienta Omicron spectrometer, model Esca^{+}, with a monochromatic Al Kα X-ray source (hν = 1486.6 eV). The spectrometer was calibrated using as binding energy references the Cu $2p_{3/2}$, Ag $3d_{5/2}$, and Au $4f_{7/2}$ peaks for pure Cu, Ag, and Au samples at 932.6 eV, 368.2 eV, and 84.0 eV, respectively. The effects of electrostatic charging on the surface were corrected using the C 1s peak of adventitious carbon from the hydrocarbon-rich environment at a binding energy of 284.8 eV as a standard. For each sample, not only the wide scan spectrum, but also the high-resolution spectra were recorded for the C 1s, O 1s, Ti 2p, Zr 3d, and Nb 3d peaks. The data analysis was performed using the Casa XPS © software.

The electrochemical polarization tests were carried out using a Gamry Reference 3000 electrochemical system using a conventional three-electrode cell with a Pt foil as counter electrode, Ag/AgCl (saturated KCl) electrode with a salt bridge as reference electrode (Ag/AgCl), and samples of the different titanium alloys as the working electrodes (0.2 cm^2 of exposed area). The measurements were taken in two naturally aerated solutions at25 °C: brine (3.5% NaCl) and Ringer (simulated body fluid). Ringer's solution is an isotonic solution with the composition of electrolytes from the extracellular fluid, which is used as a supplement of mineral salts and water for hydration, having the following composition: 8.0 g/L NaCl, 0.33 g/L CaCl2, and 0.3 g/L KCl. Before the electrochemical tests, the samples were exposed to the solutions and then subjected to open circuit conditions until a steady-state potential was reached. This procedure was accomplished in 1 h and the potential value obtained was considered the open-circuit potential (Eoc). The electrochemical polarization measurements were recorded at sweep rates of 1 mV/s, starting from a potential of -500 mV below Eoc to a potential of 1500 mVAg/AgCl. After, the polarization scan was reversed starting from a potential of 1500 mV mVAg/AgCl to a potential of 1200 mVAg/AgCl. To ensure good

reproducibility, the measurements were performed in triplicate and the average values were considered. The analyses of electrochemical polarization curves were carried out using Echem Analyst™ Software from Gamry Instruments. For comparative purposes, the corrosion current density (icorr) was estimated by means of the extrapolation of cathodic and anodic branches back to the corrosion potential (Ecorr).

The evaluation of the cell growth was performed using human umbilical cord matrix derived mesenchymal stromal cells (hUCM-MSCs) (Ethics Committee Protocol HCRP 920/2009) [49, 50]. All studies were carried out with the same cell donor. The culture medium consisted of Alpha Minimum Essential Medium (α-MEM) without phenol red, supplemented with 10 % (v/v) fetal bovine serum (FBS), penicillin (10,000 U/mL)/streptomycin (10,000 µg/mL) antibiotic solution, glucose (1 g/L), glutamine (0.365 g/L), arginine (0,435 g/L), Hepes (4.289 g/L), and sodium bicarbonate (126 g/L). A suspension of hUCM-MSCs were seeded at a density of 1.9×10^3 cells or 20000 cells/cm^2 onto each sample of TiNbZr alloy that had been previously sterilized In an autoclave at 121 °C and 14.5 psi (about 1 bar) for 30 minutes, and the alloy samples were arranged in a 24-well plate. During the experiments, a positive and negative control, corresponding to cells inoculated on a polystyrene surface of a 24-well plate and PVC sample, respectively, were used as a reference. All samples were placed into a standard incubator with 5% CO^2 at 37 °C. Cell adhesion and proliferation were examined in each sample after 4, 24, 48, and 72 h by using the MTT colorimetric method with the in vitro toxicological kit. The microcarriers were prepared according to the manufacturer's instructions and were analyzed by a Thermo Scientific spectrophotometer, model Multiskan FC, at 590 nm. After 4 h of culture 1 mL of medium was added to avoid those cells dropped on the polystyrene face of the well.

The cell morphology was analyzed by SEM after 4 and 72 h. For this purpose, the cells were initially washed in phosphate-buffered saline (PBS) at 37 °C and then fixed in 2 % (v/v) glutaraldehyde 50 % in 0.1 M cacodylate buffer and 0.1 M sucrose at 4 °C for 12 h, followed by six washes with 0.1 M cacodylate buffer. After washing, the samples were immersed in a solution of 1% osmium tetroxide and 0.1 M cacodylate buffer for 1 h. Then, the solution was replaced by tannic acid in 0.1 M cacodylate buffer for 1 h. Next, the samples were dehydrated through a graded ethanol series (30, 50, 70, 80 and 90 %) for 10 min each and three times at 100% and dried in hexamethyldisilazane. Finally, the samples were coated with gold and examined by SEM.

3. Results and Discussion

It should be pointed out that the manufacturing process of the Ti-Nb-Zr alloy samples occurred in a short period of time (solidification) and that the copper mold brought about cooling rates that could be considered high, depending on the thermal sensitivity of the alloys. These two facts would allow for the formation of metastable phases in the microstructures, similar to the homogenization process. It is important to note that in such a process the cooling occurs without the presence and interference of oxygen nor other interstitial elements; therefore, the formed phases, as well as the obtained properties, will be mainly influenced by the content of the alloy elements and cooling rates.

Figure 1 exhibits the diffractograms for the $Ti_{80}Nb_{20}$, $Ti_{75}Nb_{20}Zr_5$, $Ti_{60}Nb_{20}Zr_{20}$, $Ti_{50}Nb_{20}Zr_{30}$, and $Ti_{40}Nb_{20}Zr_{40}$ alloys. It was detected the β phase, identified by the (110), (200), (211), and (220) diffraction peaks, which coincide with the ICSD card No. 44391. Two low-intensity peaks were also detected for the $Ti_{75}Nb_{20}Zr_5$ alloy, and they are associated to the (021) and (022) diffraction planes of the martensitic α”-Ti phase. The formation of this α” phase was suppressed by higher amounts of Zr. The widening of the main (110) peak and the (200) peak for the $Ti_{80}Nb_{20}$ sample could indicate the presence of the martensitic α” phase. The peak position shifts with the increasing amount of Zr, as can be seen in Figure 2 for the (110) peak, are due to changes in the lattice parameter [48], which varies from 3.201 to 3.407 Å for the $Ti_{80}Nb_{20}$ and $Ti_{40}Nb_{20}Zr_{40}$ alloys, respectively.

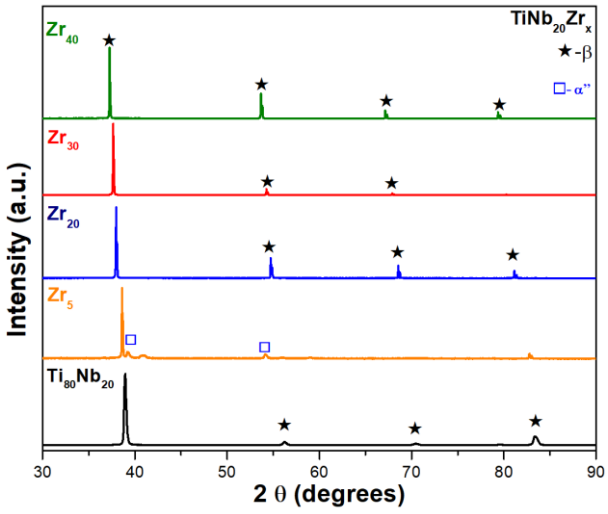

Figure 1. XRD diffractograms for the $Ti_{80}Nb_{20}$, $Ti_{75}Nb_{20}Zr_5$, $Ti_{60}Nb_{20}Zr_{20}$, $Ti_{50}Nb_{20}Zr_{30}$, and $Ti_{40}Nb_{20}Zr_{40}$ alloys.

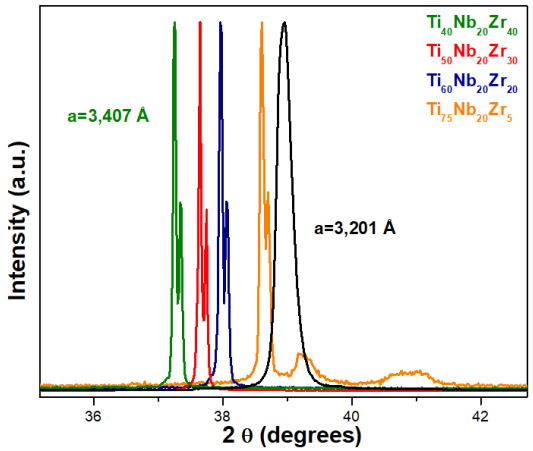

Figure 2. XRD β phase (110) peak shifts caused by the Zr addition.

Figure 3 exhibits SEM-(BSE) micrographs mode for the (a) $Ti_{80}Nb_{20}$, (b) $Ti_{75}Nb_{20}Zr_5$, (c) $Ti_{60}Nb_{20}Zr_{20}$, (d) $Ti_{50}Nb_{20}Zr_{30}$, and (e) $Ti_{40}Nb_{20}Zr_{40}$ alloys, where the presence of the martensitic α" phase was detected for both $Ti_{80}Nb_{20}$ and $Ti_{75}Nb_{20}Zr_5$ samples, corroborating the XRD results. The $Ti_{80}Nb_{20}$ alloy (Fig. 3 (a)) presents a dendritic microstructure of β phase (center of the ingot). The increase in the cooling rate, characterized by the grains oriented in the direction of the heat extraction, leads to overcoming the limit of the martensitic transformation, yielding to the formation of the α" phase within the β matrix. This result agrees with previously reported findings indicating that the increase in the cooling rate favors the growth of the martensitic phase α" for a Ti-20Nb (wt. %) alloy [51].

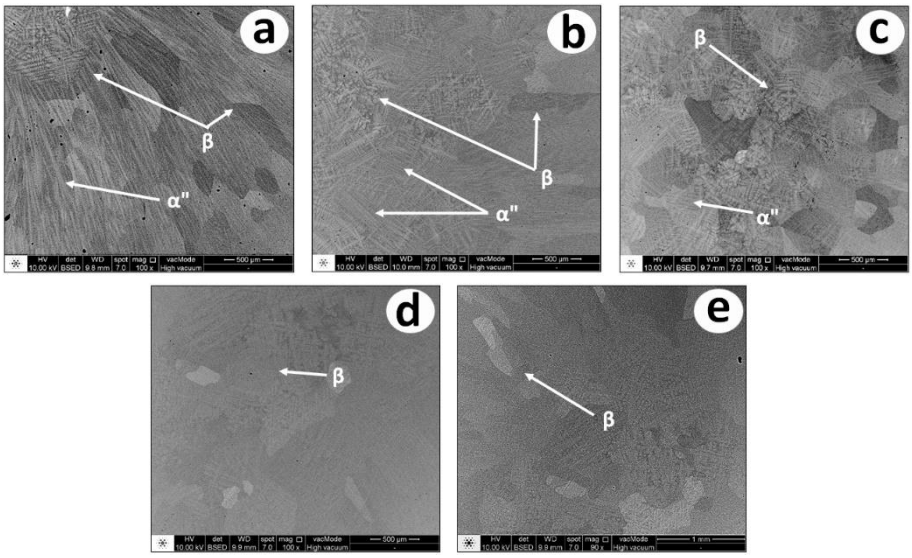

Figure 3. BSE/SEM micrographs for the (a) $Ti_{80}Nb_{20}$, (b) $Ti_{75}Nb_{20}Zr_5$, (c) $Ti_{60}Nb_{20}Zr_{20}$, (d) $Ti_{50}Nb_{20}Zr_{30}$, and (e) $Ti_{40}Nb_{20}Zr_{40}$ alloys.

The addition of Zr affects both the formed phases and the thermal sensitivity of the alloys. It can be observed in Fig. 3 (b) for the sample with 5 at.% Zr a decrease in the grains oriented in the direction of heat extraction and the appearance of equiaxial grains of the α" phase around the grains of the β phase. For the samples with 20, 30, and 40 at.% Zr, a suppression of the martensitic phase with an increase of the Zr content was observed, together with a decrease in the grains oriented in the direction of heat extraction and an increase in the equiaxial grain sizes for the β phase (Fig. 3 (c), (d), and (e)) in the center. The ω phase was not detected for any of the analyzed samples. These results are consistent with reports on the effect of the Zr addition to the Ti-Nb alloys on the suppression of both α" and ω phases [22, 29, 30, 40, 42].

The evolutions of the elastic modulus and hardness with the increase of the Zr content are shown in Table 1. In general terms, the addition of Zr causes the decreases in both the elastic modulus and hardness, according to several reports [18, 20, 21, 28, 52]; however, there are different mechanisms that could count for these decreases. The decrease in the elastic modulus for the samples with lower Zr contents (5 and 20 at. % Zr) can be attributed to the transformation of the martensitic α" phase into the β phase. The samples with 30 and 40 at. % Zr present slightly higher elastic moduli compared to the sample with 20 at. % Zr, and this can occur since Zr has an atomic radio greater than Ti and Nb, so the Zr addition to the alloy causes a lattice distortion that yields changes in the elastic modulus. In the case of hardness, a similar behavior occurs, but the martensitic phase causes a

smaller decrease in hardness as compared with the β phase samples. This could be explained by a decrease in the bonding forces by a distortion of the crystal lattice which yields the characteristics of superelasticity and superplasticity exhibited by the β-Ti alloys [10, 48, 52-55].

Table 1. Elastic modulus and hardness values for the Ti-Nb-Zr alloys.

Alloys	Elastic modulus (GPa)	Hardness (Hv)
$Ti_{80}Nb_{20}$	61.4 ± 1.1	304 ± 8
$Ti_{75}Nb_{20}Zr_5$	51.3 ± 1.0	200 ± 15
$Ti_{60}Nb_{20}Zr_{20}$	47.3 ± 0.9	230 ± 10
$Ti_{50}Nb_{20}Zr_{30}$	52.7± 1.0	253 ± 11
$Ti_{40}Nb_{20}Zr_{40}$	50.5± 0.9	248 ± 13

The chemical compositions, expressed by the Ti/(Ti+Nb+Zr), Nb/(Ti+Nb+Zr), and Zr/(Ti+Nb+Zr) atomic ratios, were obtained by EDS and XPS for the Ti-Nb-Zr alloys and are presented in Tables 2 and 3, respectively. The bulk contents assessed by EDS (Table 2), considering only the constituent metals (oxygen was also detected), present minor variations compared to the nominal values. The near-surface compositions evaluated by XPS (Table 3), considering only the constituent metals (carbon and oxygen were also detected), do not differ significantly from the bulk ones. It should be pointed out that carbon is usually detected by XPS, and it is due to adsorbed hydrocarbon molecules from the environment; oxygen also is detected, and it is due to adsorbed CO and H_2O, and metallic oxides formed on the surface [55].

Table 2. Atomic ratios obtained by EDS for the Ti-Nb-Zr alloys.

Alloy	Ti/(Ti+Nb+Zr)	Nb/(Ti+Nb+Zr)	Zr/(Ti+Nb+Zr)
$Ti_{75}Nb_{20}Zr_5$	77	18	5
$Ti_{60}Nb_{20}Zr_{20}$	59	21	20
$Ti_{50}Nb_{20}Zr_{30}$	49	20	31
$Ti_{40}Nb_{20}Zr_{40}$	40	20	40

Table 3. Atomic ratios obtained by XPS for the Ti-Nb-Zr alloys.

Alloy	Ti/(Ti+Nb+Zr)	Nb/(Ti+Nb+Zr)	Zr/(Ti+Nb+Zr)
$Ti_{75}Nb_{20}Zr_5$	77	16	7
$Ti_{60}Nb_{20}Zr_{20}$	60	16	24
$Ti_{50}Nb_{20}Zr_{30}$	54	17	29
$Ti_{40}Nb_{20}Zr_{40}$	42	17	41

High resolution XPS Ti 2p, Nb 3d, and Zr 3d, and O 1 spectra were acquired for all Ti-Nb-Zr alloy samples, and Figure 4 displays them for the $Ti_{60}Nb_{20}Zr_{20}$ sample as a representation of the behavior of all studied samples. The Ti 2p spectra were fitted with four components for each spin-orbit doublet, the Nb 3d spectra were fitted with four components, for the $Ti_{75}Nb_{20}Zr_5$ and $Ti_{60}Nb_{20}Zr_{20}$ alloys, or three components, for the $Ti_{50}Nb_{20}Zr_{30}$ and $Ti_{40}Nb_{20}Zr_{40}$ alloys, for each spin-orbit doublet, the Zr 3d spectra, with two components for each spin-orbit doublet, and the O 1s spectra, with three components for each peak. The binding energies for the Ti $2p_{3/2}$, Nb $3d_{5/2}$, and Zr $3d_{5/2}$ components are summarized in Table 4. The numbers in parenthesis are the atomic percentages of the components of each peak.

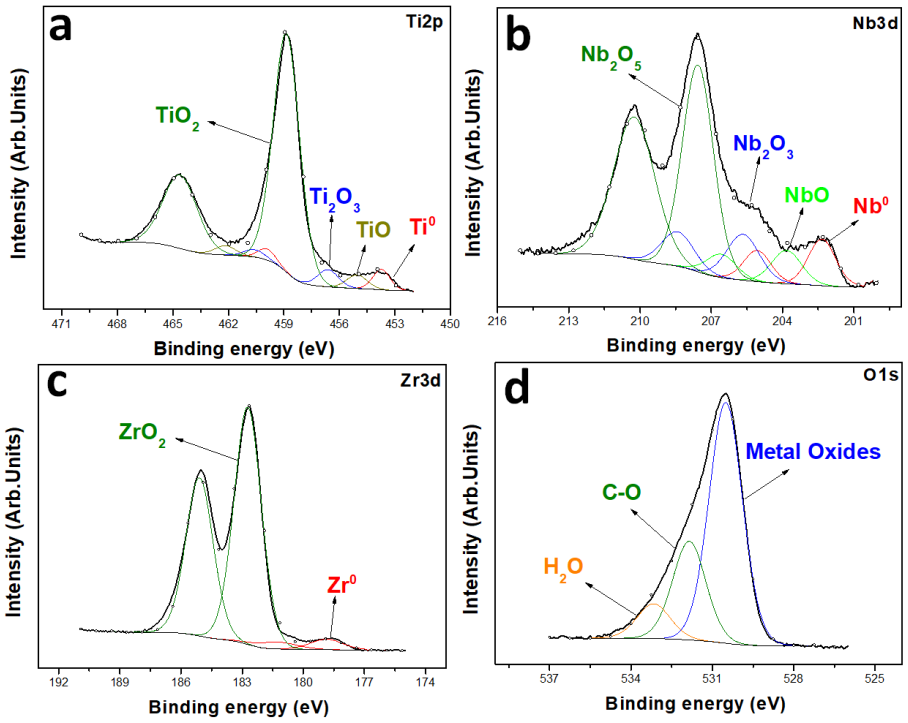

Figure 4. XPS spectra for the $Ti_{60}Nb_{20}Zr_{20}$ alloy sample: (a) Ti 2p, (b) Nb 3d, (c) Zr 3d, and (d) O 1s.

Table 4. Binding energies (in eV) obtained by XPS for the Ti-Nb-Zr alloys.

Alloy	Ti $2p_{3/2}$ BE (eV)	Nb $3d_{5/2}$ BE (eV)	Zr $3d_{5/2}$ BE (eV)
$Ti_{75}Nb_{20}Zr_5$	453.3 (4%)	202.2 (26%)	178.8 (5%)
	455.0 (3%)	203.7 (10%)	182.8 (95%)
	457.2 (20%)	205.2 (10%)	
	458.6 (73%)	207.4 (54%)	
$Ti_{60}Nb_{20}Zr_{20}$	454.2 (4%)	202.3 (11%)	178.2 (2%)
	455.9 (6%)	203.8 (9%)	182.4 (98 %)
	456.8 (6%)	205.6 (14%)	
	458.8 (84%)	207.5 (66%)	
$Ti_{50}Nb_{20}Zr_{30}$	453.5 (5%)	202.8 (5%)	178.1 (3%)
	455.5 (5%)	205.1 (4%)	182.4 (97%)
	456.9 (6%)	207.7 (91%)	
	458.6 (84%)		
$Ti_{40}Nb_{20}Zr_{40}$	454.4 (2%)	202.5 (8%)	178.6 (5%)
	455.3 (2%)	204.2 (2%)	182.9 (95%)
	456.5 (2%)	207.3 (90%)	
	459.0 (94%)		

The Ti $2p_{3/2}$ peak for each Ti-Nb-Zr alloy sample was deconvoluted into four components, as shown in Figure 4(a). The predominant component with binding energies in the range of 458.6–459.0 eV corresponds to TiO_2, the one at 456.5–457.2 eV corresponds to Ti_2O_3, the one at 455.0–455.9, to TiO, and the one at 453.3–454.4 eV, to metallic titanium (Ti^0) [56, 57]. Figure 4(b) displays the Nb 3d spectrum for the $Ti_{60}Nb_{20}Zr_{20}$ alloy having four spin-orbit doublets. The main Nb $3d_{5/2}$ component at 207.3–207.7 eV corresponds to Nb_2O_5, the one at 205.1–205.6 eV, to Nb_2O_3, the one at 203.7–204.2 eV, to NbO, and the one at 202.2–202.5 eV, to metallic niobium (Nb^0) [57]. The Zr $3d_{5/2}$ peak was fitted with two components for all four samples (Figure 4 (c)): the main one at 182.4–182.9 eV corresponds to ZrO_2 and the component at 178.1–178.8 eV, to metallic zirconium (Zr^0) [55]. The O 1s peak can be deconvoluted with three components (Figure 4(d)): the main one at

530.2–530.6 eV can be attributed to metallic oxides, the one at 531.5–532.4 eV, to adsorbed CO, and the one at 532.7–533.4 eV, to adsorbed H_2O.

These XPS results indicate that the environment affects the Ti-Nb-Zr alloys. This is evidenced by the growth of metal oxide layers on the alloy surfaces: titanium, zirconium, and, to a lesser extent, niobium oxides. The presence of low amounts of the constituent elements in the metallic state in the spectra of Figure 4 could indicate that the formed oxide layers have small thicknesses. An oxide layers is formed when the alloy surface is exposed to the atmosphere, and water is absorbed on it and forms a highly oxygenated film that attacks the alloy surface, generating the growth of oxidized film that can have its thickness increased over time, depending on the alloy reactivity [58, 59].

Subsequently, the electrochemical characterization of the Ti-Nb-Zr was carried out using a physiological Ringer's solution that simulates the environment that the medical implant materials are subjected to, and a solution that simulates the marine environment (NaCl 3.5%). Figures 5 and 6 display the typical cyclic potentiodynamic polarization curves obtained in Ringer's and NaCl solutions, respectively, for the $Ti_{80}Nb_{20}$, $Ti_{75}Nb_{20}Zr_5$, $Ti_{60}Nb_{20}Zr_{20}$, $Ti_{50}Nb_{20}Zr_{30}$, $Ti_{40}Nb_{20}Zr_{40}$ alloys.

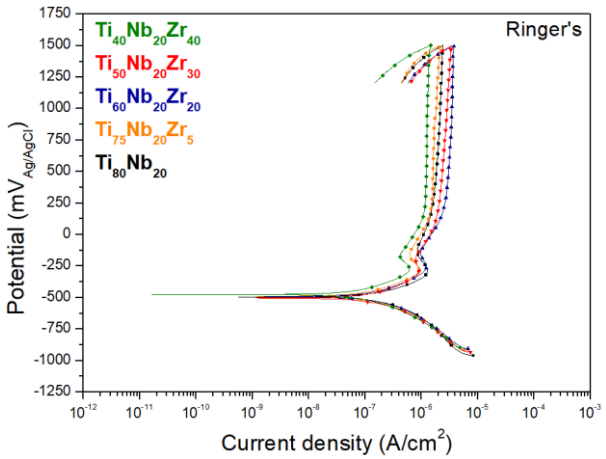

Figure 5. Cyclic potentiodynamic polarization curves for the $Ti_{80}Nb_{20}$, $Ti_{75}Nb_{20}Zr_5$, $Ti_{60}Nb_{20}Zr_{20}$, $Ti_{50}Nb_{20}Zr_{30}$, $Ti_{40}Nb_{20}Zr_{40}$ alloys immersed in Ringer's solution.

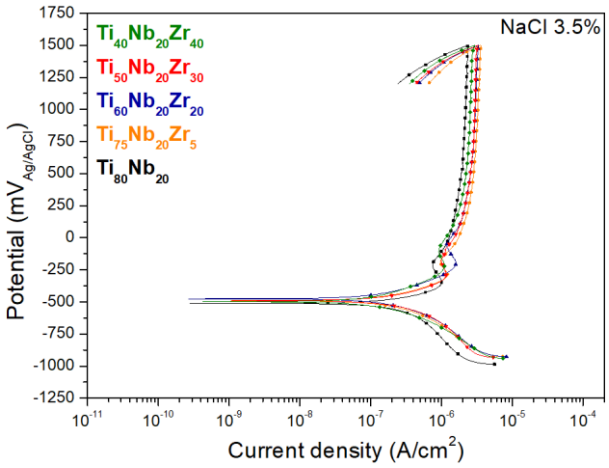

Figure 6. Cyclic potentiodynamic polarization curves for the $Ti_{80}Nb_{20}$, $Ti_{75}Nb_{20}Zr_5$, $Ti_{60}Nb_{20}Zr_{20}$, $Ti_{50}Nb_{20}Zr_{30}$, $Ti_{40}Nb_{20}Zr_{40}$ alloys immersed in NaCl solution.

In both Figures 5 and 6, the active and passive regions of the alloys exposed to the different electrolytes can be identified from the curves. The passive region is characterized by the zone where the current density remains low and almost constant. When the passivation is lost, an abrupt and significant increase in the current density occurs due to the localized breakdown of the passive film of the material by chloride ions (triggering pitting), and this zone corresponds to the pitting region. For all tested samples, a similar polarization behavior was observed for all compositions, with corrosion potential (E_{corr}) values very close to each other and broad passive regions. In addition, all samples did not present any pitting corrosion signal and remained in the passive state up to the potential value of 1500 $mV_{Ag/AgCl}$. This is well above the maximum rest electrochemical potential values reported for implant materials under *in vivo* conditions, which are of the order of +400 mV [60], and it thus indicates a high resistance to localized corrosion phenomena. This was corroborated with the negative hysteresis in the reverse scan after reaching the maximum estimated value. Table 5 summarizes the electrochemical parameters (i.e., E_{corr} and i_{corr}) determined from the potentiodynamic polarization curves for the $Ti_{80-x}Nb_{20}Zr_x$ (x = 0, 5, 10, 20, 30, and 40 at.%) alloys. Figure 7 exhibits the BSE/SEM micrographs that were obtained after the alloy samples had been submitted to the potentiodynamic cyclic tests in the Ringer's and NaCl solutions. No pitting is observed in these micrographs. These results verify the stability and self-regeneration of the passive layer of titanium and its alloys, with a broad and clear passive zone and no signs of a localized breakdown of the passive film (i.e., no pitting corrosion initiation) [61-63].

Table 5. Electrochemical parameters for the $Ti_{80-x}Nb_{20}Zr_x$ (x = 0, 5, 10, 20, 30, and 40 at.%) alloys in Ringer's and 3.4% NaCl solutions.

Alloy	Ringer		NaCl	
	E_{corr} ($mV_{Ag/AgCl}$)	I_{corr}(nA)	E_{corr} ($mV_{Ag/AgCl}$)	I_{corr}(nA)
$Ti_{80}Nb_{20}$	-4.92	1.87	-4.96	3.43
$Ti_{75}Nb_{20}Zr_5$	-4.9	2.22	-4.8	4.34
$Ti_{60}Nb_{20}Zr_{20}$	-4.97	1.99	-4.82	2.61
$Ti_{50}Nb_{20}Zr_{30}$	-4.98	1.69	-4.81	2.21
$Ti_{40}Nb_{20}Zr_{40}$	-4.96	1.33	-4.96	1.51

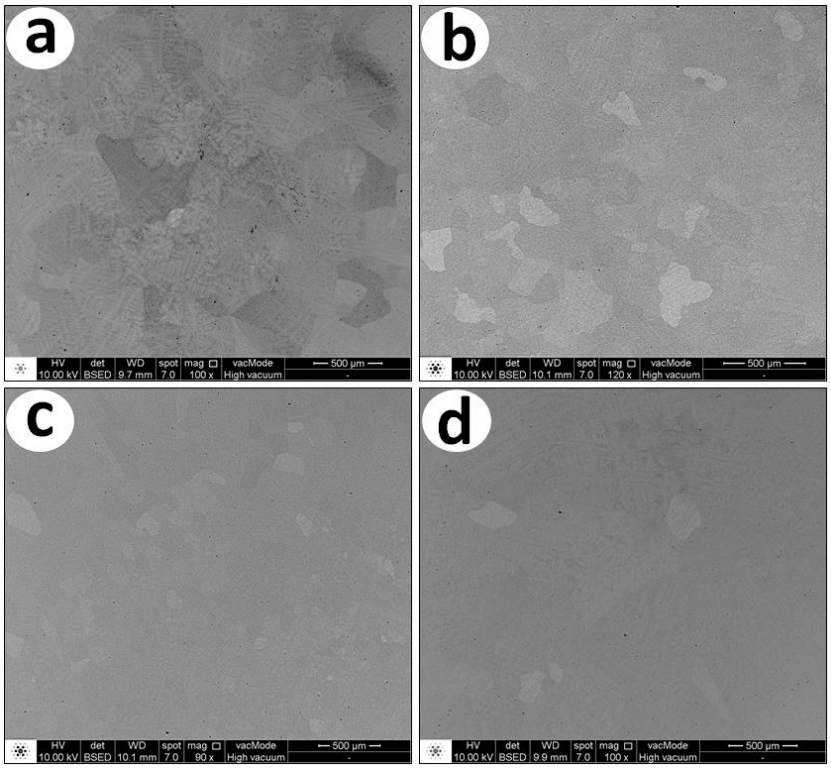

Figure 7. BSE/SEM micrographs for the (a) $Ti_{75}Nb_{20}Zr_5$ (Ringer's), (b) $Ti_{60}Nb_{20}Zr_{20}$ (NaCl), (c) $Ti_{50}Nb_{20}Zr_{30}$ (Ringer's), and (d) $Ti_{40}Nb_{20}Zr_{40}$ (3.5% NaCl) alloys obtained after the potentiodynamic polarization tests in different solutions.

The variations shown before the stabilization of the passivation region for all tested samples are due to the dissolution of the lesser stable Ti and Nb oxides that alters the characteristics of the passive layer [63, 64]. The XPS analyses carried out after the potentiodynamic cyclic tests in the Ringer's and NaCl solutions corroborate these two phenomena: the dissolution of less stable oxides and changes in the composition of the passive layers. Figure 8 displays the high resolution (a) Ti 2p, (b) Nb 3d, and (c) Zr 3d spectra for the $Ti_{60}Nb_{20}Zr_{20}$ alloy sample (the other Ti-Nb-Zr alloy samples have very similar spectra) recorded after the potentiodynamic tests in the Ringer's solution, (d) Ti 2p, (e) Nb 3d, and (f) Zr 3d spectra for the same alloy sample after the tests in the NaCl solution; these spectra are associated to only one chemical state each: TiO_2, Nb_2O_5, and ZrO_2. In contrast, the spectra shown in Figure 4 for the same sample, but recorded before the potentiodynamic tests, have peak components associated not only to those more stable oxides, but also to the metallic contributions (Ti^0, Nb^0, and Zr^0) and less stable Ti and Nb oxides. Table 6 shows the atomic ratios obtained by XPS for the Ti-Nb-Zr alloys after the potentiodynamic cyclic tests in the Ringer's and NaCl solutions, considering only the constituent metals (carbon and oxygen were also detected). The comparison of the atomic ratios in Table 6 with the values in Table 3 indicates an enrichment of both Nb and Zr, and a decrease in Ti concentration. The increase in Zr content can be explained by the free energies of the oxide formation. The ZrO_2 has the most negative value among the constituent elements, followed by TiO_2 and Nb_2O_5, respectively [63, 65-67]. Furthermore, recent studies indicate that the increasing addition of Nb in the Ti-Nb-Zr alloys improves the stability of passive layers and increases the relative proportion of all metallic oxides [63]. This would explain the proportional increase for all compositions after the corrosion tests.

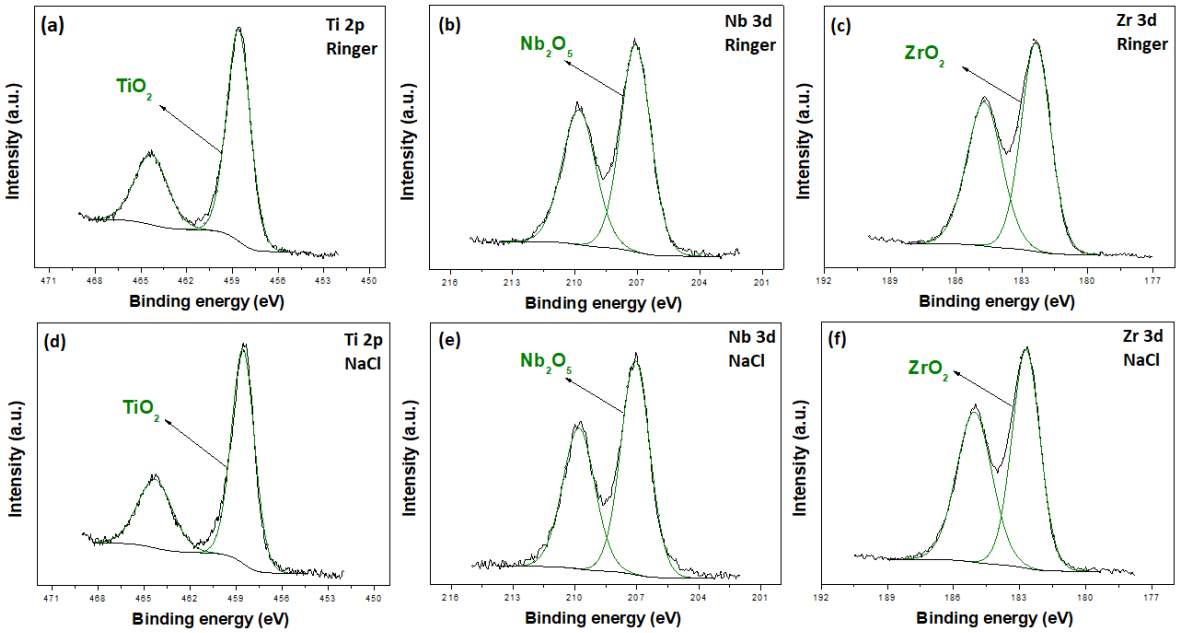

Figure 8. (a) Ti 2p, (b) Nb 3d, and (c) Zr 3d spectra for the $Ti_{60}Nb_{20}Zr_{20}$ alloy sample recorded after the potentiodynamic tests in the Ringer's solution; (d) Ti 2p, (e) Nb 3d, and (f) Zr 3d spectra for the same alloy sample after the tests in the NaCl solution.

Table 6. Atomic ratios obtained by XPS for the Ti-Nb-Zr alloys after the potentiodynamic tests in the Ringer's and NaCl solutions.

Alloy	Ti/(Ti+Nb+Zr)		Nb/(Ti+Nb+Zr)		Zr/(Ti+Nb+Zr)	
	Ringer	NaCl	Ringer	NaCl	Ringer	NaCl
$Ti_{75}Nb_{20}Zr_5$	0.59	0.60	0.31	0.29	0.10	0.11
$Ti_{60}Nb_{20}Zr_{20}$	0.43	0.39	0.28	0.29	0.29	0.32
$Ti_{50}Nb_{20}Zr_{30}$	0.33	0.29	0.28	0.30	0.39	0.41
$Ti_{40}Nb_{20}Zr_{40}$	0.25	0.25	0.24	0.26	0.51	0.49

The adhesion of mesenchymal stromal cells is one of the most important processes after inoculation, as it is essential to allow spreading and proliferation on a surface. During this process, not only the surrounding environment but also the properties of the surface are responsible for the cell adhesion and function [68, 69]. Thus, the cell adhesion and proliferation of hUCM-MSCs on Ti-Nb-Zr alloy samples and the cell morphology after 4 and 72 h of culture were analyzed. Figures 9 and 10 display BSE/SEM micrographs showing the cell morphology after 4 h (Fig.9) and 72 h (Fig.10)

of incubation for the (a) $Ti_{75}Nb_{20}Zr_5$, (b) $Ti_{60}Nb_{20}Zr_{20}$, (c) $Ti_{50}Nb_{20}Zr_{30}$, and d) $Ti_{40}Nb_{20}Zr_{40}$ alloy samples. It can be observed in Figure 9 viable cells still exhibiting a stretched and rhomboid shape with filopodia, acting as fingers that assist the adhesion and migration processes [66], which is common in healthy cells when cultured in monolayer [71]. Additionally, clusters of cells can be still observed in some surface stretches due to the inoculation being realized with a drop of cells and only after 4 h, 1 mL of medium was added. After 72 h (Fig. 10), the cells maintained their typical spindle-like morphology and already had started to proliferate and widespread onto the surface, resulting in a network pattern connecting the cells with their neighbors.

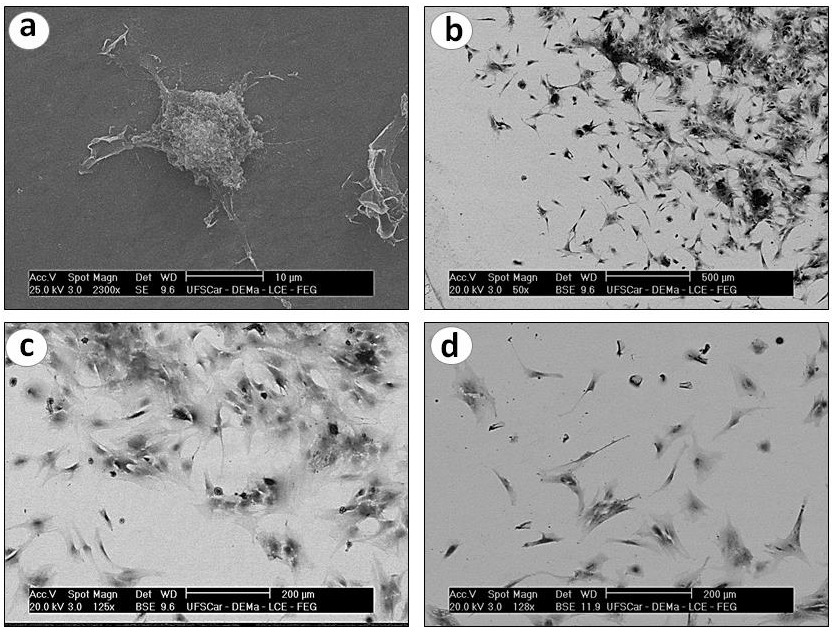

Figure 9. BSE/SEM micrographs showing the cell adhesion on the Ti-Nb-Zr alloys after 4 h of incubation: a) $Ti_{75}Nb_{20}Zr_5$, b) $Ti_{60}Nb_{20}Zr_{20}$, c) $Ti_{50}Nb_{20}Zr_{30}$, and d) $Ti_{40}Nb_{20}Zr_{40}$.

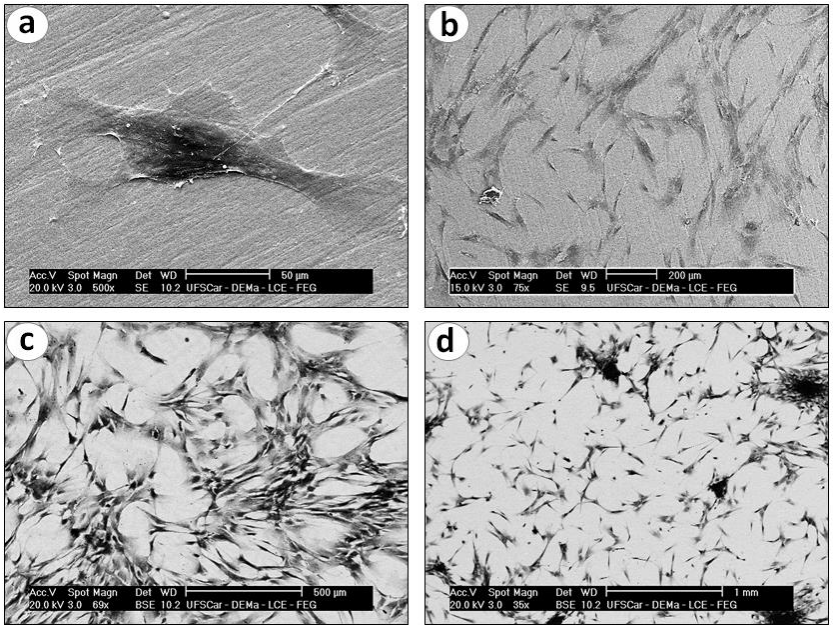

Figure 10. BSE/SEM micrographs showing the cell adhesion on the Ti-Nb-Zr alloys after 72 h of incubation: a) $Ti_{75}Nb_{20}Zr_5$, b) $Ti_{60}Nb_{20}Zr_{20}$, c) $Ti_{50}Nb_{20}Zr_{30}$, and d) $Ti_{40}Nb_{20}Zr_{40}$.

Figure 11 shows the absorbance results for the metabolically active cells on the Ti_{80-x}-Nb_{20}-Zr_x (x = 0, 5, 10, 20, 30, and 40 at.%) alloy surfaces obtained by MTT colorimetric assay after 4,24,48, and 72 h. It can be observed that the cells on all sample surfaces maintained a gradual proliferation over time; however, a drastic increment in the cell density occurred between 48 and 72 h. These results indicate that there is a relationship between the Zr content and cell growth. For Zr amounts of 5 and 20% at., there is an increase in the cell growth; however, for higher values (30 and 40% at. of Zr), there is a gradual decrease in the cell growth.

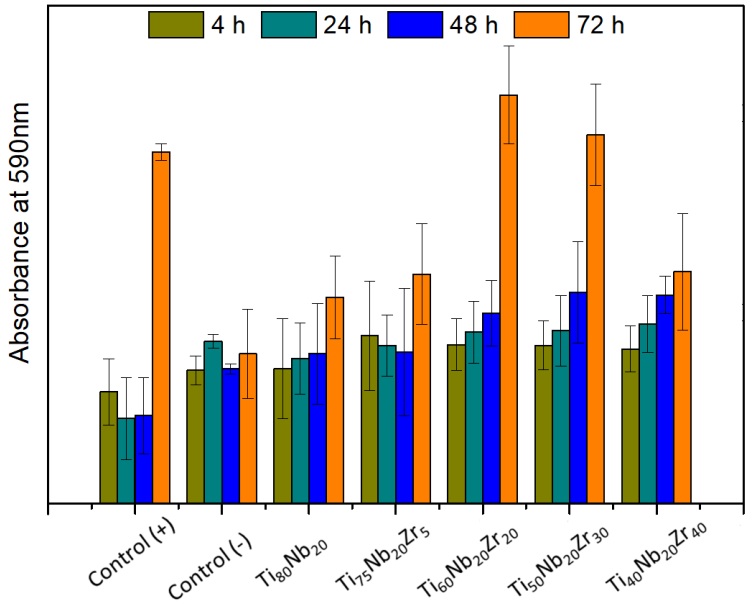

Figure 11. Absorbance results for the metabolically active cells on the alloy surfaces obtained by MTT colorimetric assay after 4, 24, 48, and 72 h.

Although zirconium oxide is considered to be biocompatible [67-69], it has an inhibitory effect on cell proliferation [71-74] since Zr^{+4} reacts with body fluids and forms zirconium phosphate on the surface instead of calcium phosphate (apatite), influencing the adsorption of proteins (integrins), which affects both growth and cell proliferation [75, 76]. Thus, the increase in the Zr content may be detrimental to the assimilation of the implant by the organism, delimiting the use of the $Ti_{50}Nb_{20}Zr_{30}$ and $Ti_{40}Nb_{20}Zr_{40}$ alloys in short-term bone fixation applications. In general, all the studied alloys showed good behavior, with the $Ti_{60}Nb_{20}Zr_{20}$ alloy presenting growth values higher than the positive control, and a satisfactory performance for the alloys with higher Zr content (30 and 40 at.%).

4. Conclusions

Ti_{80-x}-Nb_{20}-Zr_x (x = 5, 10, 20, 30, and 40 at.%) alloys were produced and characterized, and the influence of the addition of Zr on the physicochemical, electrochemical, and biological properties of the Ti-Nb_{20} alloys was investigated. The main conclusions drawn from this investigation can be summarized as follows:

(1) The addition of Zr favored the stabilization of the β phase for percentages equal or higher than 20 at.%. For both $Ti_{80}Nb_{20}$ and $Ti_{75}Nb_{20}Zr_5$ alloys, the α" phase was detected inside the β grains.

(2) The addition of Zr caused a decrease in the elastic modulus and hardness, with a minimum for the alloy with 20 at.% Zr. This decrease for the alloys with lower Zr contents was associated with the transformation of the α" phase into the β phase. Higher Zr contents induced a crystal lattice distortion that yields changes in the elastic modulus that caused a slight increase in the elastic modulus.

(3) The XPS results indicated that the environment affected the Ti-Nb-Zr alloys, and this was evidenced by the growth of metal oxide layers on the alloy surfaces: titanium, zirconium, and, to a lesser extent, niobium oxides. After the potentiodynamic cyclic tests in the Ringer's and NaCl solutions, XPS indicated the dissolution of less stable oxides and changes in the composition of the passive layers. Only the most stable oxides (TiO_2, Nb_2O_5, and ZrO_2) were detected. Enrichment of both Nb and Zr, and a depletion of Ti were revealed.

(4) The cell growth tests indicated a good performance for the alloy containing 5 at.%, a better performance for the alloy containing 20 at.%, and satisfactory performance for the alloys with higher Zr content (30 and 40 at.%).

Acknowledgements

We would like to thank Prof Conrado R. M. Afonso, from the Federal University of Sao Carlos, and the Engineer Mauricio Viera, from the Polytechnic University of Valencia, for their help. We also want to dedicate this work to the memory of Prof. Claudio A. Torres Suazo, director of the Cell Culture Laboratory of the Federal University of Sao Carlos; without his support we would not be able to finish this work. We would like to thank the Ribeirao Preto Regional Blood Center, Ribeirao Preto School of Medicine, University of Sao Paulo, Brazil, for providing the human stromal cells derived from the umbilical cord. This work was supported by the Brazilian agencies FAPESP (process 2017/25983-8) and CNPq (process 302450/2017-3). This study was financed in part by the Coordenação de Aperfeiçoamento de Pessoal de Nível Superior – Brazil (CAPES) – Finance Code 001.

References

[1] M. Niinomi, Mechanical properties of biomedical titanium alloys, Mater. Sci. Eng. A 243 (1998) 231–236.

[2] J. C. Williams, G. Lütjering, Titanium, Springer-Verlag, Berlin (2003).

[3] Y. Li, C. Yang, H. Zhao, S. Qu, X. Li, and Y. Li, New developments of Ti-based alloys for biomedical applications, Materials 7 (2014) 1709–1800.

[4] S. Gross, E. W. Abel, A finite element analysis of hollow stemmed hip prostheses as a means of reducing stress shielding of the femur, J. Biomech. 34 (2001) 995–1003.

[5] T. Ozaki, H. Matsumoto, S. Watanabe, S. Hanada, Beta Ti Alloys with Low Young' s Modulus, Mater. Trans. 45 (2004) 2776–2779.

[6] M. Niinomi, Biologically and mechanically biocompatible titanium alloys, Mater. Trans. 49 (2008) 2170–2178.

[7] R. P. Kolli, A. Devaraj, A Review of Metastable Beta Titanium Alloys, Metals 8 (2018).

[8] O. Mishchenko, O. Ovchynnykov, O. Kapstian, M. Pogorieolov, Materials 13 (2020) 1306.

[9] T. Zhang, P Ou, J. Ruan, H. Yang, J. Biomater. Appl. 35 (2021) 1284-1293.

[10] D. H. Ping, Y. Mitarai, F. X. Yin, Microstructure and shape memory behavior of a Ti-30Nb-3Pd alloy, Scr. Mater. 52 (2005) 1287-1291.

[11] Y. W. Chai, H. Y. Kim, H. Hosoda, S. Miyazaki, Self-accomodation in Ti – Nb shape memory alloys, Acta Mater. 57 (2009) 4054–4064.

[12] X. Tang, T. Ahmed, H. J. Rack, Phase transformations in Ti-Nb-Ta and Ti-Nb-Ta-Zr alloys, J. Mater. Sci. 35 (2000) 1805–1811.

[13] C. M. Lee, C. P. Ju, J. H. Chern Lin, Structure-property relationship of cast Ti-Nb alloys, J. Oral Rehabil. 29 (2002) 314–322.

[14] Y.-H. Hon, J.-Y. Wang, Y.-N. Pan, Composition/Phase Structure and Properties of Titanium-Niobium Alloys, Mater. Trans. 44 (2003) 2384–2390.

[15] J. M. Chaves, O. Florêncio, P. S. Silva Jr, P. W. B. Marques, S. G. Schneider, Anelastic relaxation associeated to phase transformations and interstitial atoms in the Ti-35Nb-7Zr alloy, J. Alloys Compd. 616 (2014) 420-425.

[16] M. Bönisch, A. Panigrahi, M. Calin, T. Waitz, M. Zehetbauer, W. Skrotzki, J. Eckert, Thermal stability and latent heat of Nb–rich martensitic Ti-Nb alloys, J. Alloys Compd. 697 (2017) 300–309.

[17] G. T. Aleixo, C. R. M. Afonso, A. A. Coelho, R. Caram, Effects of Omega Phase on Elastic Modulus of Ti-Nb Alloys as a Function of Composition and Cooling Rate, Solid State Phenom. 138 (2008) 393–398.

[18] M. Abdel-Hady, H. Fuwa, K. Hinoshita, H. Kimura, Y. Shinzato, M. Morinaga, Phase stability change with Zr content in β-type Ti–Nb alloys, Scr. Mater. 57 (2007) 1000–1003.

[19] D. Q. Martins, M. E. P. Souza, S. A. Souza, D. C. Andrade, C. M. A. Freire, R. Caram, Solute segregation and its influence on the microstructure and electrochemical behavior of Ti-Nb alloys, J. Alloys Compd. 478 (2009) 111-116.

[20] J. I. Kim, H. Y. Kim, T. Inamura, H. Hosoda, S. Miyazaki, Shape memory characteristics of Ti-22Nb-(2-8)Zr(at.%) biomedical alloys, Mater. Sci. Eng. A 403 (2005) 334–339.

[21] M. Abdel-Hady, K. Hinoshita, M. Morinaga, General approach to phase stability and elastic properties of β-type Ti-alloys using electronic parameters, Scr. Mater. 55 (2006) 477–480.

[22] J. Zhang, F. Sun, Y. Hao, N. Gozdecki, E. Lebrun, P. Vermaut, R. Portier, T. Gloriant, P. Laheurte, F. Prima, Influence of equiatomic Zr/Nb substitution on superelastic behavior of Ti-Nb-Zr alloy, Mater. Sci. Eng. A 563 (2013) 78–85.

[23] S. Prasad, M. Ehrensberger, M. P. Gibson, H. Kim, E. A. Monaco, Biomaterial properties of titanium in dentistry, J. Oral Biosci. 57 (2015) 192-199.

[24] Y.L. Hao, S.J. Li, S.Y. Sun, C.Y. Zheng, Q.M. Hu, R. Yang, Super-elastic titanium alloy with unstable plastic deformation, Appl. Phys. Lett. 87 (2005), 091906.

[25] W. Xu, X. Wu, M. Calin, M. Stoica, J. Eckert, K. Xia, Formation of an ultrafine-grained structure during equal-channel angular pressing of a β-titanium alloy with low phase stability, Scr. Mater. 60 (2009), 1012-1015.

[26] F. Sun, Y.L. Hao, S. Nowak, T. Gloriant, P. Laheurte, F. Prima, A thermo-mechanical treatment to improve the superelastic performances of biomedical Ti-26Nb and Ti-20Nb-6Zr (at.%) alloys, J. Mech. Behav. Biomed. 4 (2011) 1864-1872.

[27] E.L. Pang, E.J. Pickering, S.I. Baik, D.N. Seidman, N.G. Jones, The effect of zirconium on the

omega phase in Ti-24Nb-[0-8]Zr (at.%) alloys, Acta Mater. 153 (2018) 62-70.

[28] K.M. Kim, H.Y. Kim, S. Miyazaki, Effect of Zr content on phase stability, deformation behavior, and Young's modulus in Ti-Nb-Zr alloys, Materials 13 (2020) 476.

[29] D. Q. Martins, W. R. Osorio, M. E. P. Souza, R. Caram, A. Garcia, Effects of Zr content on microstructure and corrosion resistance of Ti-30Nb-Zr casting alloys for biomedical applications, Electrochim. Acta 53 (2008) 2809–2817.

[30] J. Málek, F. Hnilica, J. Veselý, B. Smola, K. Kolařík, J. Fojt, M. Vlach, V. Kodetová, The effect of Zr on the microstructure and properties of Ti-35Nb-XZr alloy, Mater. Sci. Eng. A 675 (2016) 1–10.

[31] M. Morinaga, M. Kato, T. Kamimura, M. Fukumoto, I. Harada, K. Kubo, Theoretical design of beta-type titanium alloys, in Titanium'92: Science and Technology, The Minerals, Metals & Materials Society, Pittsburgh, PA, USA, 1993, pp. 217-224.

[32] H. Y. M.Morinaga, Y. Murata, H.Yukawa, Molecular orbital approach to alloy design, in G. Bozzolo, R.D. Noebe, P. B. Abel (Eds.), Applied computation materials modeling: theory, simulation and experiment, Springer, New York, NY, USA, 2007, pp. 255-300.

[33] I. Weiss, S. L. Semiatin, Thermomechanical processing of beta titanium alloys—an overview, Mater. Sci. Eng. A 243 (1998) 46–65.

[34] A. Mehjabeen, W. Xu, D. Qiu, M. Qian, Redefining the β-phase stability in Ti-Nb-Zr alloys for alloy design and microstructural predicition, JOM 70 (2018) 2254-2259.

[35] Y. Zhou, Y. Li, X. Yang, Z. Cui, S. Zhu, Influence of Zr content on phase transformation, microstructure and mechanical properties of Ti75-xNb25Zrx (x = 0-6) alloys, J. Alloys Compd. 486 (2009) 628–632.

[36] F. Sun, S. Nowak, T. Gloriant, P. Laheurte, A. Eberhardt, F. Prima, Influence of a short thermal treatment on the superelastic properties of a titanium-based alloy, Scr. Mater. 63 (2010) 1053–1056.

[37] L. W. Ma, H. S. Cheng, C. Y. Chung, Effect of thermo-mechanical treatment on superelastic behavior of Ti-19Nb-14Zr (at.%) shape memory alloy, Intermetallics 32 (2013) 44–50.

[38] Q. Liu, Q. Meng, S. Guo, X. Zhao, Progress in Natural Science : Materials International α '

Type Ti – Nb – Zr alloys with ultra-low Young' s modulus and high strength, Prog. Nat. Sci. Mater. Int. 23 (2013) 1–4.

[39] S. Ozan, J. Lin, Y. Li, R. Ipek, C. Wen, Development of Ti-Nb-Zr alloys with high elastic admissible strain for temporary orthopedic devices, Acta Biomater. 20 (2015) 176–187.

[40] W. Qu, X. Sun, B. Yuan, C. Xiong, F. Zhang, Y. Li, B. Sun, Microstructures and phase transformations of Ti-30Zr-xNb (x = 5, 7, 9, 13 at.%) shape memory alloys, Mater. Charact. 122 (2016) 1–5.

[41] Q. Li, J. Li, G. Ma, X. Liu, D. Pan, Influence of ω phase precipitation on mechanical performance and corrosion resistance of Ti-Nb-Zr alloy, Mater. Des. 111 (2016) 421–428.

[42] M. T. Mohammed, Development of a new metastable beta titanium alloy for biomedical applications, Karbala Int. J. Mod. Sci. 3 (2017) 224–230.

[43] S. Ozan, J. Lin, Y. Li, Y. Zhang, K. Munir, H. Jiang, C. Wen, Deformation mechanism and mechanical properties of a thermomechanically processed β Ti–28Nb–35.4Zr alloy, J. Mech. Behav. Biomed. Mater. 78 (2018) 224–234.

[44] Y. L. Hao, S. J. Li, S. Y. Sun, R. Yang, Effect of Zr and Sn on Young's modulus and superelasticity of Ti-Nb-based alloys, Mater. Sci. Eng. A 441 (2006) 112–118.

[45] Y. Cui, Y. Li, K. Luo, H. Xu, Microstructure and shape memory effect of Ti-20Zr-10Nb alloy, Mater. Sci. Eng. A 527 (2010) 652–656.

[46] L. You, X. Song, First principles study of low Young's modulus Ti-Nb-Zr alloy system, Mater. Lett. 80 (2012) 165–167.

[47] Q. Li, M. Niinomi, M. Nakai, Z. Cui, S. Zhu, X. Yang, Effect of Zr on super-elasticity and mechanical properties of Ti-24at% Nb-(0, 2, 4)at% Zr alloy subjected to aging treatment, Mater. Sci. Eng. A 536 (2012) 197–206.

[48] H. Y. Kim, J. Fu, H. Tobe, J. Il Kim, S. Miyazaki, Crystal Structure, Transformation Strain, and Superelastic Property of Ti–Nb–Zr and Ti–Nb–Ta Alloys, Shape Mem. Superelast. 1 (2015) 107–116.

[49] J. S. da Silva, A. Mizukami, L. V. G. Gil, J. V. de Campos, O. B. G. Assis, D. T. Covas, K. Swiech C.A. T. Suazo, Improving wave-induced motion bioreactor performance for human

mesenchymal stromal cell expansion, Proc. Biochem. 84 (2019)

[50] L. V. G. Gil, H. Singh, J. S. da Silva, D. P. dos Santos, D. T. Covas, K. Swiech, C. A. T. Suazo, Feasibility of the taylor vortex flow bioreactor for mesenchymal stromal cell expansion on microcarriers, Biochem. Eng. J. 162 (2020) 107710.

[51] C. R. M. Afonso, G. T. Aleixo, A. J. Ramirez, R. Caram, Influence of cooling rate on microstructure of Ti–Nb alloy for orthopedic implants, Mater. Sci. Eng. C 27 (2007) 908–913.

[52]]Y. L. Hao, R. Yang, M. Niinomi, D. Kuroda, Y. L. Zhou, K. Fukunaga, A. Suzuki, Young's modulus and mechanical properties of Ti-29Nb-13Ta-4.6Zr in relation to α" martensite, Metall. Mater. Trans. A 33 (2002) 3137–3144.

[53] W. F. Ho, C. P. Ju, J. H. Chern Lin, Structure and properties of cast binary Ti–Mo alloys, Biomaterials 20 (1999) 2115–2122.

[54] E. S. N. Lopes, A. Cremasco, C. R. M. Afonso, R. Caram, Effects of double aging heat treatment on the microstructure, Vickers hardness and elastic modulus of Ti-Nb alloys, Mater. Charact. 62 (2011) 673–680.

[55] D. A. Tallarico, A. L. Gobbi, P. I. Paulin Filho, M. E. H Maia da Costa, P. A. P. Nascente, Growth and surface characterization of TiNbZr thin films deposited by magnetron sputtering for biomedical applications, Mater. Sci. Eng. C 43 (2014) 45-49.

[56] C. E. B. Marino, P. A. P. Nascente, S. R. Biaggio, R. C. Rocha-Filho, N. Bocchi, XPS characterization of anodic titanium oxide films grown in phosphate buffer solutions, Thin Solid Films 468 (2004) 109-112.

[57] E. D. Gonzalez, T. C. Niemeyer, C. R. M. Afonso, P. A. P. Nascente, Ti-Nb thin films deposited by magnetron sputtering on stainless steel, J. Vac. Sci. Tecnol. A 34 (2016) 021511.

[58] C.-O. A. Olsson, D. Landolt, Atmospheric oxidation of a Nb–Zr alloy studied with XPS, Corros. Sci. 46 (2004) 213–224.

[59] Y. Tanaka, M. Nakai, T. Akahori, M. Niinomi, Y. Tsutsumi, H. Doi, T. Hanawa, Characterization of air-formed surface oxide film on Ti–29Nb–13Ta–4.6Zr alloy surface using XPS and AES, Corros. Sci. 50 (2008) 2111–2116.

[60] S. N. Rosenbloom, R. A. Corbett, An assessment of ASTM F 2129 electrochemical testing of small medical implants – lessons learned, Proceedings of the NACE Corrosion Conference & Exposition, Houston, TX, USA, p 11-15, March 2007.

[61] C. Leyens, M. Peters. Titanium and Titanium Alloys; Wiley-VCH: Weinheim, Germany, 2003; ISBN 9783527602117

[62] S.D. Cramer, B.S. Covino Jr. ASM Handbook Volume 13B: Corrosion: Materials; ASM International: Materials Park, OH, USA, 2005; Volume 13, ISBN 087170708X.

[63] P. F. Ji, B. Li, B. H. Chen, F. Wang, W. Ma, X. Y. Zhang, M. Z. Ma, R. P. Liu, Effect of Nb addition on the stability and biological corrosion resistance of Ti-Zr alloy passivation films, Corros. Sci. 170 (2020) 108696.

[64] Y. Yan (Editor), Bio-tribocorrosion in biomaterials and medical implants, Woodhead Publishing, 2013.

[65] B. A. Green, H. M. Meyer, R. S. Benson, Y. Yokoyama, P. K. Liaw, C. T. Liu, A study of the corrosion behaviour of Zr50Cu(40-X)Al10PdX bulk metallic glasses with scanning Auger microanalysis, Corros. Sci. 50 (2008) 1825–1832.

[66] Q. P. Cao, S. Peng, X. N. Zhao, X. D. Wang, D. X. Zhang, J. Z. Jiang, Effect of Nb substitution for Cu on glass formation and corrosion behavior of Zr-Cu-Ag-Al-Be bulk metallic glass, J. Alloys Compd. 683 (2016) 23-31.

[67] F. Colmenero, A. M. Fernández, J. Cobos, V. Timón, Temperature-Dependent Gibbs Free Energies of Reaction of Uranyl-Containing Materials Based on Density Functional Theory, J. Phys. Chem. C 122 (2018) 5268–5279.

[68] B. Ladoux, A. Nicolas, Physically based principles of cell adhesion mechanosensitivity in tissues, Rep. Prog. Phys. 75 (2012) 1–25.

[69] B. Venugopal, P. Mogha, J. Dhawan, A. Majumder, Cell density overrides the effect of substrate stiffness on human mesenchymal stem cells' morphology and proliferation, Biomater. Sci. 6 (2018) 1109–1119.

[70] K. Chang, J. Baginski, S. F. Hassan, M. Volin, D. Shukla, V. Tiwari, Filopodia and viruses: An analysis of membrane processes in entry mechanisms, Front. Microbiol. 7 (2016) 1–13.

[71] A. K.-L. Chen, S. Reuveny, S. K. W. Oh, Application of human mesenchymal and pluripotent stem cell microcarrier cultures in cellular therapy: Achievements and future direction, Biotechnol. Adv. 31 (2013) 1032–1046.

[72] Y. Li, C. Wong, J. Xiong, P. Hodgson, C. Wen, Cytotoxicity of titanium and titanium alloying elements, J. Dent. Res. 89 (2010) 493–497.

[73] S. Sista, C. Wen, P. D. Hodgson, G. Pande, The influence of surface energy of titanium-zirconium alloy on osteoblast cell functions in vitro, J. Biomed. Mater. Res. A 97 (2011) 27–36.

[74] F. Y. Zhou, B. L. Wang, K. J. Qiu, W. J. Lin, L. Li, Y. B. Wang, F. L. Nie, Y. F. Zheng, Microstructure, corrosion behavior and cytotoxicity of Zr-Nb alloys for biomedical application, Mater. Sci. Eng. C 32 (2012) 851–857.

[75] J. Hallab, N., Anderson, S., Caicedo, M., Jacobs, Zirconium and Niobium Affect Human Osteoblasts, Fibroblasts, and Lymphocytes in a Similar Manner to More Traditional Implant Alloy Metals, J. ASTM Int. 3 (2006) 1–12.

List of Tables

List of Figures

Figure 9. BSE/SEM micrographs showing the cell adhesion on the Ti-Nb-Zr alloys after 4 h of incubation: a) $Ti_{75}Nb_{20}Zr_5$, b) $Ti_{60}Nb_{20}Zr_{20}$, c) $Ti_{50}Nb_{20}Zr_{30}$, and d) $Ti_{40}Nb_{20}Zr_{40}$.

Figure 10. BSE/SEM micrographs showing the cell adhesion on the Ti-Nb-Zr alloys after 72 h of incubation: a) $Ti_{75}Nb_{20}Zr_5$, b) $Ti_{60}Nb_{20}Zr_{20}$, c) $Ti_{50}Nb_{20}Zr_{30}$, and d) $Ti_{40}Nb_{20}Zr_{40}$.

Figure 11. Absorbance results for the metabolically active cells on the alloy surfaces obtained by MTT colorimetric assay after 4, 24, 48, and 72 h.